

MAY 2004

***The Influence of Idealized Heterogeneity on Convective  
Planetary Boundary Layers Coupled to the Land Surface***

Edward G. Patton  
Peter P. Sullivan  
Chin-Hoh Moeng

## NCAR TECHNICAL NOTES

The Technical Note series provides an outlet for a variety of NCAR Manuscripts that contribute in specialized ways to the body of scientific knowledge but that are not suitable for journal, monograph, or book publication. Reports in this series are issued by the NCAR scientific divisions. Designation symbols for the series include:

*EDD – Engineering, Design or Development Reports*

Equipment descriptions, test results, instrumentation, and operating and maintenance manuals.

*IA – Instruction Aids*

Instruction manuals, bibliographies, film supplements, and other research, or instructional aids.

*PPR – Program Progress Reports*

Field program reports, interim and working reports, survey reports, and plans for experiments.

*PROC – Proceedings*

Documentation or symposia, colloquia, conferences, workshops, and lectures. (Distribution may be limited to attendees.)

*STR – Scientific and Technical Reports*

Data compilations, theoretical and numerical investigations, and experimental results.

*The National Center for Atmospheric Research (NCAR) is operated by the nonprofit University Corporation for Atmospheric Research (UCAR) under the sponsorship of the National Science Foundation. Any opinions, findings, conclusions, or recommendations expressed in this publication are those of the author(s) and do not necessarily reflect the views of the National Science Foundation.*

# The influence of idealized heterogeneity on convective planetary boundary layers coupled to the land surface

Edward G. Patton<sup>1</sup>, Peter P. Sullivan, and Chin-Hoh Moeng  
*National Center for Atmospheric Research*

<sup>1</sup>*Corresponding address:* Edward G. Patton, MMM Division, NCAR, P.O. Box 3000, Boulder, CO 80307-3000. *email:* patton@ucar.edu, *phone:* 303-497-8958



# Contents

<b>1</b>	<b>Introduction</b>	<b>1</b>
<b>2</b>	<b>Land-Atmosphere Coupling</b>	<b>5</b>
<b>3</b>	<b>The LSM</b>	<b>9</b>
<b>4</b>	<b>Simulations</b>	<b>13</b>
<b>5</b>	<b>Verification</b>	<b>17</b>
5.1	Comparison to previous studies . . . . .	17
5.2	Evaluation of lateral domain size . . . . .	18
<b>6</b>	<b>Results</b>	<b>21</b>
6.1	Instantaneous fields and statistics . . . . .	21
6.1.1	Instantaneous fields . . . . .	21
6.1.2	Bulk boundary layer statistics . . . . .	25
6.1.3	Horizontally averaged statistics . . . . .	31
6.2	Phase-averaged fields . . . . .	35
6.2.1	Definition of averaging procedures and nomenclature . . . . .	35
6.2.2	Influence of varying $\lambda/z_i$ on the land surface . . . . .	36
6.2.3	Influence of varying $\lambda/z_i$ on heterogeneity-induced PBL fields . . . . .	40
6.2.4	Profiles of $x$ -averaged phase-correlated fields . . . . .	47
6.2.5	Impact of organized motions on point measurements . . . . .	56
<b>7</b>	<b>Summary and Conclusions</b>	<b>63</b>
<b>A</b>	<b>Numerics</b>	<b>65</b>



# Preface

This report describes the development of a coupled model and the evaluation of the influence of that coupling by way of an investigation of heterogeneous surface forcing on convective planetary boundary layer dynamics. This document was previously submitted as two separate manuscripts to the *Journal of the Atmospheric Sciences*. A reviewer suggested that the two manuscripts were too detailed and that a condensed single manuscript might be more appropriate for the Journal, with a more detailed description of the study published as an NCAR Technical Note. We concur with this suggestion and hope that this Technical Note which combines the two manuscripts into one detailed exposition will be useful for those interested in the topic.

Edward Patton  
Peter Sullivan  
Chin-Hoh Moeng





# List of Figures

3.1	Time evolution of the four vertical levels of soil moisture and temperature from the 1-D off-line LSM run initialized from measurements from Little Washita at 11:30 LST on Day 193 of SGP97. Initial soil conditions for the LSM for the <i>wet</i> and <i>dry</i> coupled simulations are taken at noon seven days apart. . . .	10
4.1	Initial profiles of potential temperature ( $\theta$ ) and water vapor mixing ratio ( $q$ ) for the dry PBL (DP) and wet PBL (WP) cases. . . . .	14
5.1	Comparison of velocity variances ( $\mathbf{u} = \langle u'^2 + \frac{2}{3}e \rangle / w_*^2$ , $\mathbf{w} = \langle w'^2 + \frac{2}{3}e \rangle / w_*^2$ , and $\mathbf{SGS} = \frac{2}{3}\langle e \rangle / w_*^2$ ) derived from the current coupled LES-LSM code (solid lines) and those measured in the tank experiments of Willis and Deardorff (1974) case S1 ( $\times, \bullet$ ) and the LES results of Schmidt and Schumann (1989) (dashed line). Note that the bold typeface does not imply a vector quantity. The SGS energy ( $e$ ) predicted by the LES is assumed isotropic such that one-third is added to each of velocity variances. . . . .	18
5.2	Comparison of horizontal velocity two-point correlations [ $R_{uu}(\Delta y)$ ] versus increasing lag in the lateral direction ( $\Delta y$ ) for three cases that are identical to case DP-15S except for the lateral extent of the domain. The second panel depicts vertical profiles of the square root of the horizontally- and time-averaged horizontal velocity variance normalized by $w_*$ for the same three cases. . . .	19
6.1	Instantaneous ( $x, y$ ) slices of surface fluxes (sensible, latent and soil heat fluxes) and the corresponding soil temperature and moisture at the uppermost vertical level in the LSM ( $z = -2.5$ cm, which represents the vertical average over the top five centimeters in the soil) from DP-AS at the last time step in the simulation. . . . .	22

6.2	Instantaneous two dimensional slices of vertical velocity and water vapor mixing ratio at the first time step used in the averaging for case DP-AS (top two panels). The third panel depicts the coincident surface forcing (H, LE, -G) determined via the LES-LSM coupling. The lowest panel is the volumetric soil moisture at the uppermost soil level, $z = -2.5$ cm. . . . .	23
6.3	The same as Figure 6.2, except for case DP-7.5S. . . . .	24
6.4	Variation of the horizontally- and time-averaged surface exchange coefficients for momentum and heat ( $C_m$ and $C_h$ ) versus the normalized heterogeneity wavelength ( $\lambda/z_i$ ) for both the DP and WP cases. The line with symbols represents the heterogeneous soil cases. The solid, dashed and dotted lines with no symbols are the homogeneous soil cases. . . . .	27
6.5	Boundary-layer and time averaged turbulence kinetic energy normalized by $w_*^2$ versus the normalized heterogeneity wavelength ( $\lambda/z_i$ ) for both the DP and WP cases. The line with symbols represents the heterogeneous soil cases. The solid, dashed and dotted lines with no symbols are the homogeneous soil cases. . . . .	29
6.6	Time evolution of the horizontally averaged boundary layer height ( $z_i$ ) for all cases over the complete averaging period for both the DP and WP cases. Lines by themselves represent heterogeneous cases. Lines with symbols represent homogeneous cases. . . . .	29
6.7	Normalized entrainment rates ( $w_e/w_*$ ) versus the normalized heterogeneity wavelength ( $\lambda/z_i$ ) for both the DP and WP cases. The line with symbols represents the heterogeneous soil cases. The solid, dashed and dotted lines with no symbols are the homogeneous soil cases. . . . .	30
6.8	Vertical profiles of normalized horizontal velocity variance, $(\langle u''^2 \rangle + \frac{2}{3}\langle e \rangle)/w_*^2$ , for both the DP and WP cases. Lines by themselves represent heterogeneous cases. Lines with symbols represent homogeneous cases. The variable $e$ is the subgrid-scale energy as predicted by the LES. . . . .	32
6.9	Vertical profiles of normalized vertical velocity variance, $(\langle w''^2 \rangle + \frac{2}{3}\langle e \rangle)/w_*^2$ , for both the DP and WP cases. Lines by themselves represent heterogeneous cases. Lines with symbols represent homogeneous cases. . . . .	32

- 6.10 Vertical profiles of normalized vertical flux of water vapor mixing ratio ( $\langle w''q'' + \tau_{wq} \rangle / (w_* \Theta_*)$ ) for both the DP and WP cases. Lines by themselves represent heterogeneous cases. Lines with symbols represent homogeneous cases.  $\tau_{wq}$  is the subgrid-scale vertical mixing ratio flux predicted by the subgrid-scale model. . . . . 33
- 6.11 Vertical profiles of normalized vertical flux of virtual potential temperature ( $\langle w''\theta_v'' + \tau_{w\theta_v} \rangle / (w_* \theta_{v*})$ ) for both the DP and WP cases. Lines by themselves represent heterogeneous cases. Lines with symbols represent homogeneous cases.  $\tau_{w\theta_v}$  is the subgrid-scale vertical virtual potential temperature flux predicted by the subgrid-scale model. . . . . 34
- 6.12 The  $x/\lambda$  variation of phase-correlated soil temperature,  $T_p$  (K, left column), and phase-correlated soil moisture,  $\Theta_p$  (% , right column) for cases DP-30S (top row), DP-7.5S (middle row), and DP-3S (bottom row). Each panel presents results at the four soil levels in the LSM (solid:  $z = -2.5$  cm, dotted:  $z = -12.5$  cm, dashed:  $z = -40$  cm, dash-dot:  $z = -80$  cm). The hatches demarcate the  $x/\lambda$  extent of the *wet* soil. . . . . 37
- 6.13 Phase-correlated sensible ( $H_p$ ), latent ( $LE_p$ ), and soil ( $G_p$ ) surface heat fluxes over the *wet* soil (left) and *dry* soil (right) for cases DP-30S (dotted)  $\lambda/z_i = 18$ , DP-7.5S (solid)  $\lambda/z_i = 4$  and DP-3S (dashed)  $\lambda/z_i = 1$ . . . . . 39
- 6.14 Normalized phase-correlated horizontal velocity ( $u_p/w_*$ , left column) and vertical velocity ( $w_p/w_*$ , right column) as a function of  $x/\lambda$  and  $z/z_i$  for cases DP-30S (top), DP-7.5S (middle), and DP-3S (bottom). The dashed-line is the phase-averaged boundary layer depth,  $z_{ip}$ ; dotted contours represent negative phase-correlated values; and the hatches demarcate the  $x/\lambda$  extent of the *wet* soil. . . . . 41
- 6.15 Normalized phase-correlated virtual potential temperature ( $\theta_{vp}/\theta_{v*}$ , left column) and water vapor mixing ratio ( $q_p/\Theta_*$ , right column) as a function of  $x/\lambda$  and  $z/z_i$  for cases DP-30S (top row), DP-7.5S (middle row), and DP-3S (bottom row). All markings on the figures are the same as those defined in Figure 6.14. Note the change in magnitude for the different cases. . . . . 42

- 6.16 Normalized phase-correlated vertical virtual potential temperature fluxes,  $w_p\theta_{vp}/(w_*\theta_{v*})$  (left column) and vertical water vapor mixing ratio flux,  $w_pq_p/(w_*\Theta_*)$  (right column) as a function of  $x/\lambda$  and  $z/z_i$  for cases DP-30S (top), DP-7.5S (middle), and DP-3S (bottom). All markings on the figures are the same as those defined in Figure 6.14. . . . . 45
- 6.17 Normalized phase-correlated horizontal virtual potential temperature fluxes,  $u_p\theta_{vp}/(w_*\theta_{v*})$  (left column), and horizontal water vapor mixing ratio fluxes,  $u_pq_p/(w_*\Theta_*)$  (right column), as a function of  $x/\lambda$  and  $z/z_i$  for cases DP-30S (top), DP-7.5S (middle), and DP-3S (bottom). All markings on the figures are the same as those defined in Figure 6.14. . . . . 46
- 6.18 Normalized phase-correlated water vapor mixing ratio,  $q_p/\Theta_*$  (left column) and phase-correlated vertical water vapor mixing ratio flux,  $w_pq_p/(w_*\Theta_*)$  (right column) as a function of  $x/\lambda$  and  $z/z_i$  for cases WP-30S (top), WP-7.5S (middle), and WP-3S (bottom). All markings on the figures are the same as those defined in Figure 6.14. . . . . 48
- 6.19 The normalized  $x$ -average of the square of the phase-correlated horizontal velocity ( $[u_p^2]/w_*^2$ ) and vertical velocity ( $[w_p^2]/w_*^2$ ) for all cases with heterogeneity. The left hand panels depict DP cases and the right hand panels WP cases. . . . . 49
- 6.20 The normalized  $x$ -average of phase-correlated virtual potential temperature ( $[|\theta_{vp}|]/\theta_{v*}$ ) and water vapor mixing ratio ( $[|q_p|]/\Theta_*$ ) for all cases with heterogeneity. The left hand panels depict DP cases and the right hand panels WP cases. . . . . 51
- 6.21 The normalized  $x$ -average of phase-correlated vertical virtual potential temperature flux ( $[w_p\theta_{vp}]/(w_*\theta_{v*})$ ) and vertical water vapor mixing ratio flux ( $[w_pq_p]/(w_*\Theta_*)$ ) for all cases with heterogeneity. The left hand panels depict DP cases and the right hand panels WP cases. . . . . 52
- 6.22 Vertical profiles of normalized total virtual heat flux ( $\langle w''\theta_v'' \rangle + \langle \tau_{w\theta_v} \rangle / (w_*\theta_{v*})$ ), the phase-correlated virtual heat flux  $[w_p\theta_{vp}]/(w_*\theta_{v*})$ , and background turbulent virtual heat flux ( $\langle w'\theta_v' \rangle + \langle \tau_{w\theta_v} \rangle / (w_*\theta_{v*})$ ) for six cases. The left column are the DP cases, and the right column are the WP cases. The top row are the 30S cases, middle row are the 7.5S cases and the bottom row are the 3S cases. . . . . 54

- 6.23 Vertical profiles of normalized total vertical mixing ratio flux  $(\langle w''q'' \rangle + \langle \tau_{wq} \rangle) / (w_* \Theta_*)$ , the phase-correlated mixing ratio flux  $[w_p q_p] / (w_* \Theta_*)$ , and background turbulent mixing ratio flux  $([w'q'] + \langle \tau_{wq} \rangle) / (w_* \Theta_*)$  for six cases. The left column are the DP cases, and the right column are the WP cases. The top row are the 30S cases, middle row are the 7.5S cases and the bottom row are the 3S cases. . . . . 55
- 6.24 Vertical profiles of normalized phase-correlated vertical velocity  $(w_p/w_*, \bullet)$ , and time-averaged vertical velocity  $(\{w\}/w_*, \square)$  at fixed  $x/\lambda$  for case DP-7.5S. The (top-left, top-right, lower-left, lower-right) panels represent locations  $x/\lambda = (0 \text{ or } 1, 0.25, 0.5, 0.75)$ . The hatch marks demarcate plus and minus one standard deviation of  $w_p/w_*$  from the  $y$ -average. Note the scale difference on the abscissa of the  $x/\lambda = 0.75$  plot. . . . . 57
- 6.25 Vertical profiles of normalized vertical virtual potential temperature flux for case DP-7.5S. The  $\times$ -profile represents the the total flux,  $(\langle w''\theta_v'' \rangle + \langle \tau_{w\theta_v} \rangle) / (w_* \theta_{v*})$ . The  $\bullet$ -profile presents the background turbulent contribution,  $\langle w'\theta_v' \rangle_{y,t} / (w_* \theta_{v*})$ , and the hatch marks demarcate plus and minus one standard deviation of  $\langle w'\theta_v' \rangle_{y,t} / (w_* \theta_{v*})$  from the  $y$ -average. The  $\square$ -profile is the time-average at each  $x/\lambda$  and  $z/z_i$  location at  $y = L_y/2$ . The (top-left, top-right, lower-left, lower-right) panels represent locations  $x/\lambda = (0 \text{ or } 1, 0.25, 0.5, 0.75)$ . See the discussion in Section 6.2.5 for further explanation of how these quantities are calculated. . . . . 59
- 6.26 Vertical profiles of normalized vertical water vapor mixing ratio flux for case DP-7.5S. The  $\times$ -profile represents the the total flux,  $(\langle w''q'' \rangle + \langle \tau_{wq} \rangle) / (w_* \Theta_*)$ . The  $\bullet$ -profile presents the background turbulent contribution,  $\langle w'q' \rangle_{y,t} / (w_* \Theta_*)$ , and the hatch marks demarcate plus and minus one standard deviation of  $\langle w'q' \rangle_{y,t} / (w_* \Theta_*)$  from the  $y$ -average. The  $\square$ -profile is the time-average at each  $x/\lambda$  and  $z/z_i$  location at  $y = L_y/2$ . The (top-left, top-right, lower-left, lower-right) panels represent locations  $x/\lambda = (0 \text{ or } 1, 0.25, 0.5, 0.75)$ . See the discussion in Section 6.2.5 for further explanation of how these quantities are calculated. . . . . 60



# List of Tables

4.1	Bulk properties for all cases. The quantities are: $z_i$ , the PBL height; $\lambda/z_i$ , the ratio of the scale of the heterogeneity ( $\lambda$ ) to the PBL height; $w_*$ , the convective velocity; $H$ , the surface sensible heat flux ( $= \rho C_p w_* \theta_*$ ); $LE$ , the surface latent heat flux ( $= \rho L w_* \Theta_*$ ); $G$ , the soil heat flux; $\theta_{v*}$ , the total surface buoyancy flux ( $= \langle w''\theta'' \rangle + 0.61 \theta_* \langle w''q'' \rangle$ ); $\beta$ , the Bowen ratio ( $H/LE$ ). These bulk quantities are averaged horizontally over all space and over the entire averaging period. The angle brackets denoting this averaging process are omitted for convenience. $n/a$ stands for <i>not applicable</i> since $\lambda$ is undefined for the homogeneous cases. . . . .	15
-----	---	----





# Abstract

This report describes the development and results of numerical experiments investigating the influence of 2-30 km strip-like heterogeneity on wet and dry convective boundary layers coupled to the land surface. The strip-like heterogeneity is shown to dramatically alter the structure of the free-convective boundary layer by inducing significant organized circulations that modify turbulent statistics. The coupling with the land-surface modifies the circulations compared to previous studies using fixed surface forcing. Total boundary layer turbulence kinetic energy increases significantly for surface heterogeneity at scales between  $\lambda/z_i = 4$  and 9, however entrainment rates for all cases are largely unaffected by the strip-like heterogeneity.

A conditional sampling technique, based on the scale of the surface heterogeneity (phase averaging), is used to identify and quantify the organized surface fluxes and motions in the atmospheric boundary layer. The impact of the organized motions on turbulent transport depends critically on the scale of the heterogeneity  $\lambda$ , the boundary layer height  $z_i$  and the initial moisture state of the boundary layer. Dynamical and scalar fields respond differently as the scale of the heterogeneity varies. Surface heterogeneity of scale  $4 < \lambda/z_i < 9$  induces the strongest organized flow fields ( $u_p, w_p$ ) while heterogeneity with smaller or larger  $\lambda/z_i$  induces little organized motion. However, the organized components of the scalar fields (virtual potential temperature and mixing ratio) grow continuously in magnitude and horizontal scale, as  $\lambda/z_i$  increases. For some cases, the organized motions can contribute nearly 100% of the total vertical moisture flux. Patch-induced fluxes are shown to dramatically impact point measurements that assume the time-average vertical velocity to be zero. The magnitude and sign of this impact depends on the location of the measurement within the region of heterogeneity.



# Chapter 1

## Introduction

Land-atmosphere coupling is widely recognized as a crucial component of regional, continental and global scale numerical models. Predictions from these large-scale models are sensitive to small-scale surface layer processes like heat and moisture fluxes at the air-soil-vegetation interface as well as boundary layer treatments (*e.g.*, Garratt, 1993). The soil moisture boundary condition has a considerable influence on medium- to long-range weather forecasts and on simulated monthly mean climatic states (*e.g.*, Rowntree and Bolton, 1983). Heterogeneous soil moisture conditions can occur at many scales both naturally (Mahrt et al., 2001a) and through human modification (Weaver and Avissar, 2001). Naturally occurring heterogeneity can arise through a number of mechanisms such as spatially varying soil or vegetation type and human-induced heterogeneity can result from spatially-varying agricultural practices that vary from farmer to farmer. Both types of heterogeneity can introduce dramatic variability in boundary layer surface forcing.

There have been a number of prior investigations into the effects of non-homogeneous surface forcing on the PBL using high-resolution large eddy simulation (LES) (*e.g.*, Hechtel et al., 1990; Hadfield et al., 1991; Shen and Leclerc, 1995; Avissar and Schmidt, 1998; Albertson and Parlange, 1999; Albertson et al., 2001; Raasch and Harbusch, 2001; Esau and Lyons, 2002; Kustas and Albertson, 2003). Hechtel et al. (1990) used measurements to drive a relatively coarse resolution LES and found no significant modifications to homogeneous cases which they attributed to having a mean wind in their simulation. Hadfield et al. (1991) studied relatively small-scale (1.5 and 4.5 km wavelength) strip-like heterogeneity under free convective conditions and found that the heterogeneity induced organized motions in the PBL. These motions increased horizontal and vertical velocity variances near the upper/lower boundaries and in the mid-PBL, respectively. Shen and Leclerc (1995)

and Raasch and Harbusch (2001) showed that for small-scale patch-like heterogeneity, the intensity of the organized motions increased when the horizontal-scale of the heterogeneity increased to about the PBL height. When investigating land-surface forcing that is fixed in time, Avissar and Schmidt (1998) found larger-scale heterogeneity to continually intensify the organized motions when the heterogeneity increased from two to forty kilometers. Rather than specify the surface fluxes, which completely decouples the forcing from the overlying atmosphere, Albertson and Parlange (1999), Albertson et al. (2001), and Kustas and Albertson (2003) investigated land-surface heterogeneity using specified surface temperature and moisture. However, none of these studies used a dynamically coupled system where the soil responds to the atmosphere and vice versa. In addition, these studies are typically of relatively coarse resolution ( $12.5 \text{ m} \leq \Delta x \leq 100 \text{ m}$ , and  $20 \text{ m} \leq \Delta z \leq 50 \text{ m}$ ) and, with the exception of Avissar and Schmidt (1998), focused on relatively small-scale heterogeneity (*e.g.*,  $250 \text{ m} \leq \lambda \leq 5 \text{ km}$ ). In our view, the shortcomings and sensitivities exhibited by large-scale numerical models are a consequence of both the inadequate modeling of the PBL and poor representation of the interaction with the land surface. In order to improve existing parameterizations, a more complete understanding of the mechanics and thermodynamics of air-soil interaction and the transport of water vapor by turbulent processes in the PBL are required.

Point measurements are potentially impacted by landscape-induced organized motions (Finnigan et al., 2003). To properly evaluate the surface energy balance, Mahrt (1998) suggests that the vertical flux associated with stationary eddies (which is systematically missed in current point measurement practices) must be included. Mahrt (1998) also mentions that the influence of this stationary eddy flux diminishes when the observational level is closer to the surface. An understanding of precisely how these motions affect measurements is lacking, yet such an understanding is required for proper interpretation of observations.

This paper examines the interactions between the atmosphere and the land surface using an LES model for the PBL coupled to a land surface model (LSM). Fine grids and large computational domains are used to examine the impact of a range of soil heterogeneity scales ( $\lambda = 2\text{-}30 \text{ km}$ ) on PBL turbulence and the vertical flux of water vapor mixing ratio. The coupling between the PBL and the land-surface is found to be of fundamental importance in determining the PBL response. The heterogeneity is shown to influence the PBL differently depending on the moisture content of the PBL air. We use phase-averaging to investigate the influence of the heterogeneity-scale on the the organized motions that develop. The contribution from these induced motions to the total vertical flux of virtual potential temperature

and water vapor mixing ratio is quantified. In addition, the impact of these motions on point measurements taken at various locations within the heterogeneity is elucidated.



## Chapter 2

# Land-Atmosphere Coupling

Over land surfaces during daytime hours, the surface energy balance (SEB) is thermodynamically coupled to the growth of the boundary layer through interactions between the surface sensible and latent heat fluxes, the atmospheric temperature and humidity and the growth rate of the boundary layer by entrainment (Raupach, 2000). Through the SEB, incoming solar radiation absorbed at the ground is partitioned to determine the energy available to the coupled land-atmosphere system. Key entities involved in the SEB, such as heat and water vapor fluxes, are influenced by PBL concentrations of these quantities which themselves are influenced by their surface fluxes, forming a negative feedback loop (McNaughton and Raupach, 1996).

The main focus of this research is on the PBL, but in an attempt to incorporate these important feedbacks in the study, we coupled our well-established 3D, time-dependent, LES code (Sullivan et al., 1996) to the NOAH (National Center for Environmental Prediction / Oregon State University / Air Force / Office of Hydrology) LSM, version 2.0 (Chang et al., 1999). Numerous models of varying sophistication and empiricism have been proposed to describe the physics of soil-water-vegetation systems. Our choice of the NOAH model is based on the following desirable features: 1) the straightforward manner with which it can be coupled with a parent atmospheric model, 2) only a few empirical constants are needed to describe the land surface, 3) its good predictive capabilities, and 4) the robustness of the model itself.

The LES predicts three-dimensional and time-dependent velocity fields  $(u, v, w)$  by numerically integrating a filtered set of incompressible Navier-Stokes equations under the Boussinesq approximation. To incorporate buoyancy effects, the LES also integrates a thermodynamic energy equation  $(\theta)$  and an equation for water vapor mixing ratio  $(q)$ , which

are combined to calculate virtual potential temperature ( $\theta_v = \theta + 0.61\theta q$ ). The effects of unresolved motions in the LES are estimated by following an equation for subgrid-scale (SGS) energy ( $e$ ). In the soil, the LSM (NOAH) predicts vertical profiles of temperature ( $T$ ) and moisture ( $\Theta$ ), by integrating a 1-D set of the soil thermodynamic and hydrologic equations (Mahrt and Pan, 1984; Pan and Mahrt, 1987). At every  $(x, y)$  grid point, the lower boundary conditions for the LES and the upper boundary conditions for the LSM define the coupling between the PBL and the land-surface. Atmospheric velocity boundary conditions are determined through dynamically calculating a drag coefficient from a prescribed surface roughness length and the wind field at the first LES grid level, while surface temperature and moisture boundary conditions are determined dynamically at every grid point by solving the SEB. See Appendix A for other numerical details of the code.

The SEB for an infinitesimally thin layer at the ground surface can be written (following Brutsaert, 1982; Chang et al., 1999):

$$R_n = H + LE + G + Misc \quad (2.1)$$

where radiation fluxes toward the surface are taken as positive and all other fluxes are considered positive when leaving the surface. This sign convention is loosely based on the premise that radiation drives the energy of the surface and that the other energy fluxes are the means by which the surface disposes of the absorbed radiation. In Equation (2.1),  $R_n$  is the net radiation, which can be broken down into the sum of its parts:  $R_n = R_s(1 - \alpha) + \epsilon R_{dn} - \epsilon \sigma T_s^4$ , where  $R_s$  is the incoming solar radiation,  $\alpha$  is the albedo of the surface,  $\epsilon$  is the surface emissivity,  $R_{dn}$  is the downwelling long-wave radiation,  $\sigma$  is the Stefan-Boltzman constant, and  $T_s$  is the surface temperature.  $H$  is the sensible heat flux, parameterized as  $-\rho C_p C_h U(\theta_a - \theta_s)$  where  $\rho$  is the air density,  $C_p$  is the specific heat of the air,  $C_h$  is an exchange coefficient for heat,  $U$  is the wind speed immediately above the surface, and  $\theta_a$  and  $\theta_s$  are the potential temperature of the air and ground surface respectively.  $LE$  is the latent heat flux, parameterized as  $-\rho L C_e U(q_a - q_s)$  where  $L$  is the latent heat of vaporization,  $C_e$  is an exchange coefficient for vapor, and  $q_a$  and  $q_s$  are water vapor mixing ratio of the air and ground surface respectively.  $G$  is the soil heat flux which can be parameterized as  $k_T(\Theta_1) \frac{T_s - T_1}{z_1}$ , where  $k_T(\Theta_1)$  is the soil thermal conductivity that depends on the soil moisture  $\Theta_1$  at the first soil level  $z_1$  and soil type. *Misc.* represents other terms such as contributions from precipitation, melting snow, horizontal advection, or storage, which we ignore. Dynamically, the atmosphere and land-surface are coupled through the surface momentum flux. The surface momentum flux is parameterized as  $\tau = \rho u_*^2 = \rho C_m U^2$ , where



$u_*$  is the friction velocity and  $C_m$  is the drag coefficient. Through dynamic calculation of  $\tau$ ,  $R_n$ ,  $H$ ,  $LE$ , and  $G$  the atmosphere is therefore directly coupled to the land-surface.

This coupling is also a natural mechanism to undertake an investigation into the influence of land-surface heterogeneity on PBL structure. It is known that under free convective (no wind) conditions, imposed land-surface heterogeneity induces organized atmospheric motions (*e.g.*, Hadfield et al., 1991), but how these organized motions feed back to dry/cool the soil, and how that drying/cooling influences the organized motions has yet to be established. In the horizontal, landscape heterogeneity has been shown to influence the PBL structure at scales up to 40 km (Avissar and Schmidt, 1998). However, the typical  $(x,y,z)$  domain of LES studies of the PBL to date is about  $5 \times 5 \times 2 \text{ km}^3$  (*e.g.*, Moeng, 1984; Hadfield et al., 1991). Therefore, in order to incorporate heterogeneous land-surface forcing in our simulations, it is imperative that we consider computational domains and time-scales that are large compared to those routinely considered in LES of the PBL. Therefore, an LES that utilizes adequate resolution to capture turbulence and at the same time covers a large horizontal domain requires large numbers of grid points. For example, in a  $30 \times 5 \times 3 \text{ km}^3$  domain,  $9 \times 10^6$  grid points are required for a mesh size of  $50 \times 50 \times 20 \text{ m}^3$ .



## Chapter 3

# The LSM: Deployment, Input Parameters, and Initial Conditions

The LSM is implemented at every  $(x, y)$  grid point in the LES. Each of these grid points is covered by perennial grasses, with a roughness length for momentum  $z_{om}$  of 0.1 m, and overlays four silty clay loam soil layers at depths of [0.05, 0.20, 0.60, 1.00] m. Since the surface is covered by grasses, we assume a constant surface albedo of 0.2 across the domain for all cases. All snow and ice components of the LSM are turned off. The exchange coefficients for momentum, heat, and moisture ( $C_m, C_h, C_e$ ) are evaluated locally at every timestep based on Paulson's (1970) similarity functions.  $C_h$  and  $C_e$  are assumed equal.

In the LSM, the parameter  $c_z$  defines the relationship between the roughness height for momentum  $z_{om}$  and the roughness height for heat  $z_{oh}$ :

$$z_{oh} = z_{om} e^{-(258 c_z \kappa u_* z_{om})}. \quad (3.1)$$

To determine the value of  $c_z$ , following Brutsaert (1982) we assume that the exchange coefficients for momentum ( $C_m$ ) and heat ( $C_h$ ) are related by the expression:  $C_m/C_h \sim 3$ , which is valid for bluff bodies (see Figure 5.4, Brutsaert, 1982). Assuming the drag law to be applicable, we know that  $C_m = u_*^2/U^2$  and  $C_h = \theta_*/(\Delta\theta U)$ . Therefore  $C_m/C_h = \ln(z_{om}/z_{oh})$ , or  $z_{om}/z_{oh} = e^3$ . Substituting into Equation (3.1) gives  $c_z = 0.1$ . This is different from the default value ( $c_z=0.2$ ) in NOAH thereby increasing the efficiency of surface scalar exchange compared to NOAH's default, but is derived directly from an understanding of land-surface exchange at the scale of interest.

In addition to modifying  $c_z$ , the LSM needed another modification to be applicable for the relatively small-scale application discussed here. As it was obtained from the National

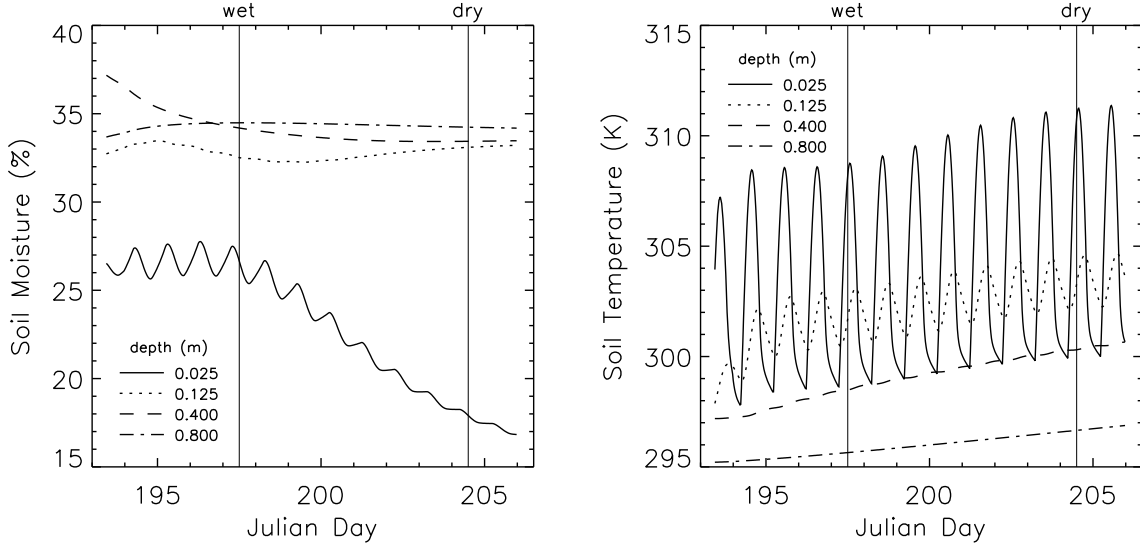


Figure 3.1: Time evolution of the four vertical levels of soil moisture and temperature from the 1-D off-line LSM run initialized from measurements from Little Washita at 11:30 LST on Day 193 of SGP97. Initial soil conditions for the LSM for the *wet* and *dry* coupled simulations are taken at noon seven days apart.

Centers for Environmental Prediction (NCEP), the LSM assumes the convective scaling velocity  $[w_* = \langle \frac{g}{\rho} z_i (\frac{H}{\theta_o C_p} + 0.61E) \rangle^{1/3}]$  is the minimum wind speed to avoid singular solutions under zero wind (free convection) conditions. While this assumption may be reasonable for the larger-scale flows where the PBL is not resolved,  $w_*$  is a bulk PBL parameter and would therefore decouple the soil from the local overlying atmosphere. To remain consistent with our adopted coupling method (through drag law assumptions), we assume a local drag law formulation to determine a small convective velocity scale following Schmidt and Schumann (1989) such that the minimum wind speed at the ground surface is dynamically calculated from the following:

$$u_{min} = 0.07 \left( \frac{g}{\theta_o} \Delta z C_h \Delta \theta_v \right)^{1/3} \quad (3.2)$$

where,  $g$  is the gravitational acceleration,  $\theta_o$  is a reference temperature,  $\Delta z$  is the distance between the ground and the first grid point above the surface,  $C_h$  is the exchange coefficient for heat derived by the LSM and  $\Delta \theta_v$  is the virtual potential temperature gradient between the same two heights.

Initial soil conditions were taken from ground-based measurements at the Little Washita site on Day 193 of the Southern Great Plains 1997 (SGP97) experiment. This day and location were chosen because nearly an inch of rain fell on the preceding 1.5 days and they

coincided with an intensive observing period. The observations were interpolated to the four soil levels in the LSM. Before using these as initial conditions for the LES-LSM runs, the soil model was run off-line for four complete diurnal cycles to allow the LSM to equilibrate. The noon-time conditions after these four diurnal cycles were used as the *wet* initial soil conditions (Figure 3.1). It is important to note that these *wet* initial soil conditions are such that the evaporation will be determined by a combination of the available soil moisture and the atmospheric demand rather than at the evaporative potential rate. *Dry* soil conditions were obtained by running the off-line LSM further for another seven diurnal cycles allowing the soil to dry under realistic forcing. Noon-time conditions after the seven day dry down period were chosen as *dry* conditions (Figure 3.1). *Average* initial soil conditions were obtained by picking the noon-time soil conditions that provided surface fluxes nearly equal to the noon-time fluxes averaged every day over the entire one-week dry-down period.



# Chapter 4

## Simulations

The coupled LES-LSM simulations employ (600,100,144) grid points in the  $(x,y,z)$  directions representing a (30,5,2.88) km domain. This leads to a grid spacing of (50,50,20) meters in each of the  $(x,y,z)$  directions.

A geostrophic wind of  $0 \text{ m s}^{-1}$  is imposed in both  $x$  and  $y$  directions, therefore the simulations are in the free convection limit. The only external forcing imposed on the system is specified through the incoming solar radiation, which is set to  $700 \text{ W m}^{-2}$  and is constant in time for all cases.

For all of the simulations, the initial potential temperature is constant with height (300K) below 790m. A capping inversion is imposed (3K/0.1km) between 790 m and 890 m, and the middle of this layer we call the initial inversion height,  $z_i = 840 \text{ m}$ ; above 890 m the stratification is  $3 \text{ K/km}$  (Figure 4.1).

Two different PBLs are simulated with varying moisture content. In the first set of cases, the PBL was initialized dry ( $1 \text{ g kg}^{-1}$ ) throughout the entire domain (DP, dry PBL). The second set of cases was initialized with a relatively wet atmosphere ( $8 \text{ g kg}^{-1}$ ) in the PBL, dropping sharply to  $1 \text{ g kg}^{-1}$  across the initial inversion layer, between 790 and 840 m (WP, wet PBL). See Figure 4.1 for a visual representation of the initial DP and WP conditions.

For each of the DP and WP cases, nine simulations were performed. Three of these are horizontally homogeneous cases with uniform soil conditions that are *wet* (WS), *dry* (DS), and *average* (AS) respectively. The subsequent six cases are initialized with horizontally heterogeneous soil conditions. The heterogeneity that is imposed occurs solely in the  $x$ -direction as a step-function change between *wet* and *dry* soil. We define  $\lambda$  as the wavelength of one complete *wet* and *dry* cycle. The wavelengths vary as  $\lambda = [2, 3, 5, 7.5, 15, 30] \text{ km}$ . At initial times, the  $x$ -extent of a single patch ( $\lambda/2$ ) ranges therefore from  $1.2z_i$  to  $17.8z_i$ . The

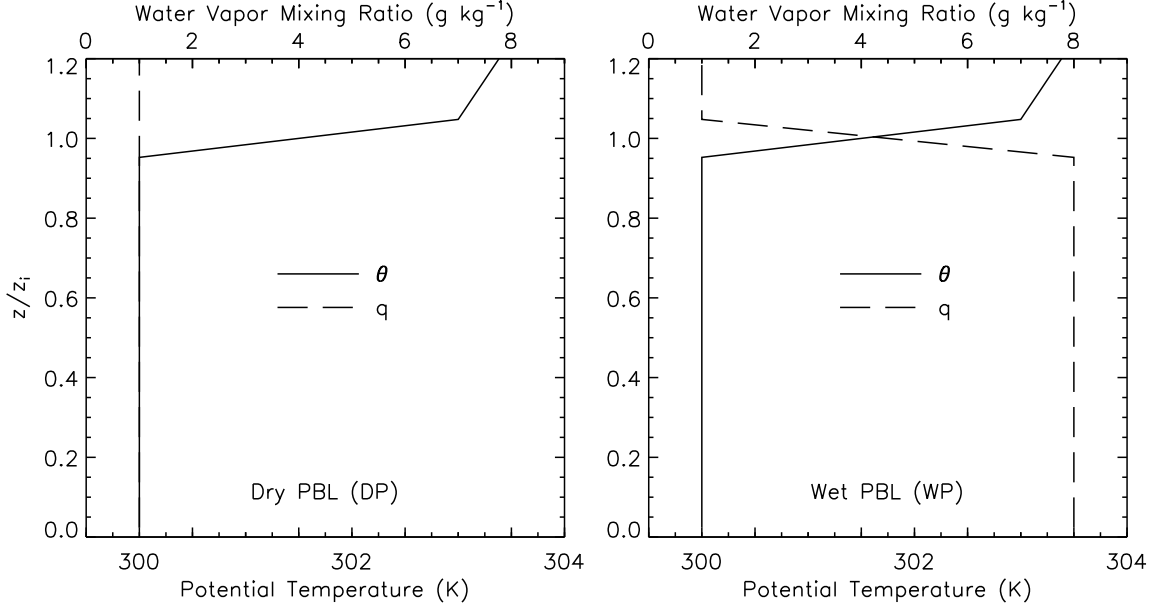


Figure 4.1: Initial profiles of potential temperature ( $\theta$ ) and water vapor mixing ratio ( $q$ ) for the dry PBL (DP) and wet PBL (WP) cases.

soil conditions are homogeneous in the  $y$ -direction for all simulations.

The nomenclature used to discuss the cases from here on will adhere the following format: The case name includes a description of the initial PBL moisture content followed by a description of the underlying soil conditions (separated by a hyphen). For example, case DP-WS refers to the run which was initiated with a *dry* PBL and a horizontally homogeneous *wet* soil condition, and case WP-7.5S refers to the case initialized with a *wet* PBL and a  $\lambda = 7.5$  km wavelength heterogeneous soil condition. The rest of the names follow accordingly (see Table 4.1).

Each simulation is integrated out in time until the turbulence is in equilibrium with its external forcing. This time is defined by the necessary time for the boundary layer averaged turbulence kinetic energy and the boundary layer growth rate to become nearly constant. These criteria were typically satisfied within (2.8-3.3, 1.9-2.5) hours for the (DP, WP) cases, respectively. The time steps for these simulations were variable but ranged between (0.7-1.6, 1.4-1.7) s. Therefore, the simulations were integrated for about (6000, 4000) time steps before any averaging began. Statistics were calculated over the subsequent 4000 time steps, or about (4-9, 8-10) turnover times, where a turnover time  $t_*$  is defined as  $z_i/w_*$ . For normalization purposes, we define  $\theta_* = H/(\rho C_p w_*)$ ,  $\Theta_* = E/(\rho w_*)$  and  $\theta_{v*} = (\frac{H}{C_p} + 0.61 \theta_* E)/(\rho w_*)$ . See Table 4.1 for the horizontally- and time-averaged values of these quantities.



Case	$z_i$ (km)	$\lambda/z_i$	$w_*$ (m s <sup>-1</sup> )	$H$ (W m <sup>-2</sup> )	$LE$ (W m <sup>-2</sup> )	$G$ (W m <sup>-2</sup> )	$\theta_{v*}$ (m K s <sup>-1</sup> )	$\beta$
DP-WS	1.66	n/a	2.35	259.42	138.97	80.98	0.23	1.87
DP-DS	1.85	n/a	2.69	358.74	25.32	78.22	0.32	14.17
DP-AS	1.79	n/a	2.58	326.70	59.91	81.26	0.29	5.45
DP-30S	1.71	17.55	2.52	311.00	83.41	77.82	0.27	3.73
DP-15S	1.75	8.56	2.54	312.61	84.30	76.46	0.28	3.71
DP-7.5S	1.73	4.33	2.52	310.51	83.94	78.59	0.27	3.70
DP-5S	1.72	2.91	2.51	308.05	82.97	80.90	0.27	3.71
DP-3S	1.74	1.72	2.51	307.14	82.56	80.94	0.27	3.72
DP-2S	1.74	1.15	2.51	308.05	82.86	79.83	0.27	3.72
WP-WS	1.67	n/a	2.37	264.72	133.73	80.68	0.23	1.98
WP-DS	1.79	n/a	2.67	361.68	23.77	77.20	0.32	15.22
WP-AS	1.76	n/a	2.58	329.94	56.80	81.12	0.29	5.81
WP-30S	1.70	17.61	2.52	315.22	79.73	76.92	0.28	3.95
WP-15S	1.70	8.82	2.52	316.11	80.53	75.96	0.28	3.93
WP-7.5S	1.72	4.37	2.53	315.62	80.78	76.69	0.28	3.91
WP-5S	1.72	2.91	2.52	312.61	79.76	79.71	0.28	3.92
WP-3S	1.72	1.74	2.52	311.43	78.88	80.48	0.28	3.95
WP-2S	1.73	1.55	2.52	312.05	79.02	79.73	0.28	3.95

Table 4.1: Bulk properties for all cases. The quantities are:  $z_i$ , the PBL height;  $\lambda/z_i$ , the ratio of the scale of the heterogeneity ( $\lambda$ ) to the PBL height;  $w_*$ , the convective velocity;  $H$ , the surface sensible heat flux ( $= \rho C_p w_* \theta_*$ );  $LE$ , the surface latent heat flux ( $= \rho L w_* \Theta_*$ );  $G$ , the soil heat flux;  $\theta_{v*}$ , the total surface buoyancy flux ( $= \langle w'' \theta'' \rangle + 0.61 \theta_* \langle w'' q'' \rangle$ );  $\beta$ , the Bowen ratio ( $H/LE$ ). These bulk quantities are averaged horizontally over all space and over the entire averaging period. The angle brackets denoting this averaging process are omitted for convenience. *n/a* stands for *not applicable* since  $\lambda$  is undefined for the homogeneous cases.



## Chapter 5

### Verification

As mentioned above, large numbers of grid points are required to investigate desired scale range of heterogeneity while maintaining the ability to resolve the response of important PBL scales of motion. Therefore, before performing the land-surface coupling, the NCAR LES code was ported from a shared memory (Cray vector supercomputer) environment to a distributed memory massively parallel (*e.g.*, IBM SP3 supercomputer) environment using the Message Passing Interface (MPI). A single MPI decomposition in the vertical direction is used, which is natural since finite differences are employed in the vertical direction and a spectral representation in the horizontal directions. Initial tests of the new code indicate that the code scales well, *i.e.*, the wall clock time decreases linearly as the number of MPI processes increases (not shown). Each simulation discussed in this manuscript took about (54,45) wall clock hours for the (DP, WP) cases on 48 IBM SP3 CPUs, or about (2592, 2160) CPU hours. In order to achieve acceptable efficiency in the coupled LES-LSM, it was also necessary to parallelize the LSM portion of the code across all MPI tasks.

#### 5.1 Comparison to previous studies

Before embarking towards an extensive study with the newly developed coupled LES-LSM, tests were performed to verify that results generated were comparable to previous research. The investigation presented by Schmidt and Schumann (1989) is considered the first to examine the free convective PBL in a robust and concise manner. The same case as Schmidt and Schumann (1989) was run with the new code. The main difference between the simulations is that the current simulation uses a coupled land-surface boundary condition. Through 1-D off-line LSM testing we devised a set of soil conditions and incoming solar radiation that

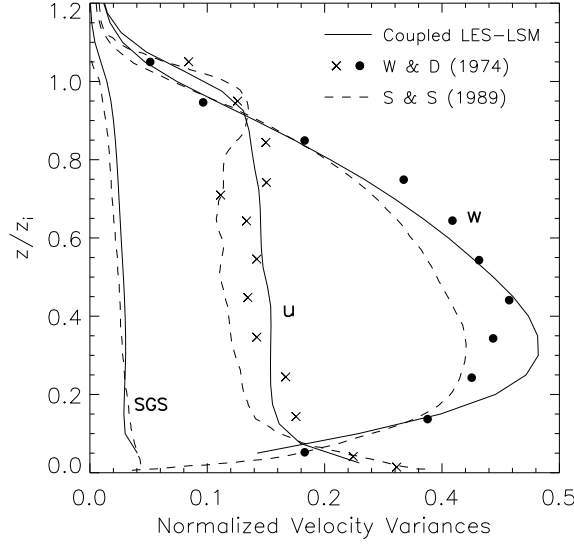


Figure 5.1: Comparison of velocity variances ( $\mathbf{u} = \langle u'^2 + \frac{2}{3}e \rangle / w_*^2$ ,  $\mathbf{w} = \langle w'^2 + \frac{2}{3}e \rangle / w_*^2$ , and  $\mathbf{SGS} = \frac{2}{3}\langle e \rangle / w_*^2$ ) derived from the current coupled LES-LSM code (solid lines) and those measured in the tank experiments of Willis and Deardorff (1974) case S1 ( $\times, \bullet$ ) and the LES results of Schmidt and Schumann (1989) (dashed line). Note that the bold typeface does not imply a vector quantity. The SGS energy ( $e$ ) predicted by the LES is assumed isotropic such that one-third is added to each of velocity variances.

would provide surface fluxes similar to those imposed in Schmidt and Schumann (1989). Measurements from the Willis and Deardorff (1974) tank experiments provide observational support.

The variances and SGS energy from the coupled code are slightly larger in magnitude through the majority of the PBL than those of Schmidt and Schumann (1989) (Figure 5.1), which is consistent with the comparison of these codes presented in Nieuwstadt et al. (1993). Notable, however, is that the current coupled code outperforms Schmidt and Schumann (1989) code at reproducing the turbulent statistics from the Willis and Deardorff (1974) tank experiments. These results provide confidence that incorporating the LSM at the lower boundary and porting the code to massively parallel machines has not dramatically altered the performance of the code.

## 5.2 Evaluation of lateral domain size

The imposed heterogeneity varies only in the  $x$ -direction, not in  $y$ . Therefore, we utilize a large domain in the  $x$ -direction and a relatively small domain in the  $y$ -direction. It is

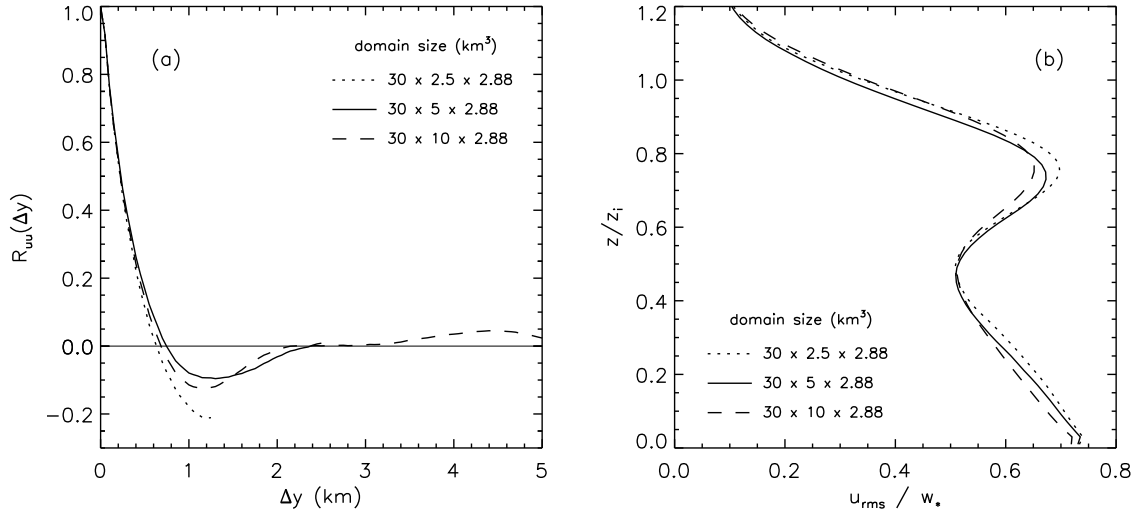


Figure 5.2: Comparison of horizontal velocity two-point correlations  $[R_{uu}(\Delta y)]$  versus increasing lag in the lateral direction ( $\Delta y$ ) for three cases that are identical to case DP-15S except for the lateral extent of the domain. The second panel depicts vertical profiles of the square root of the horizontally- and time-averaged horizontal velocity variance normalized by  $w_*$  for the same three cases.

prudent to evaluate whether the relatively short lateral extent of the domain influences the flow that ensues. If the  $y$ -domain is too small, the organized motions that develop will become artificially coupled through the periodic boundary conditions. To evaluate whether our domain choice is large enough to represent that of an infinite domain, two additional simulations were performed. These cases are identical to case DP-15S except that the  $y$ -domain is either halved or doubled. Therefore, the two cases utilize 50 or 200 nodes to represent 2.5 or 10 km in  $y$ , respectively. We chose to evaluate the DP-15S case since the heterogeneity strongly influenced the statistics (to be shown in Section 6.1).

Following the analysis of Komminaho et al. (1996), too small a domain should reveal itself through amplification of two-point horizontal velocity correlations  $[R_{uu}(\Delta y)]$  with increasing lag in the lateral direction ( $\Delta y$ ). Comparison of  $R_{uu}$  (Figure 5.2a) suggests that halving the domain size amplifies the lateral correlation of horizontal velocity (most noticeable at  $\Delta y = 1.2$  km). Doubling the size of the lateral dimension has some impact on the correlations, slightly increasing the amplitude at  $\Delta y = 1.2$  km and minimally decreasing the lateral distance corresponding to the first zero-crossing. Vertical profiles of normalized horizontal root-mean-square velocities ( $u_{rms}/w_*$ , where  $u_{rms} = \langle u'^2 + \frac{2}{3}e \rangle^{1/2}$ ) confirm that the extent of the lateral domain has little influence on predicted turbulence statistics (Figure

5.2b). Therefore, through this analysis we are reasonably confident that our domain choice of  $30 \times 5 \times 2.88 \text{ km}^3$  does not adversely influence the quantitative results and adequately represents simulations of heterogeneity that infinitely span the lateral dimension.

# Chapter 6

## Results

### 6.1 Instantaneous fields and statistics

#### 6.1.1 Instantaneous fields

##### *6.1.1.1 Horizontally varying land-surface properties and forcing*

As an example, instantaneous horizontal slices of land surface properties from the last time step of simulation DP-AS (Figure 6.1) show evidence of the coupling between the PBL and the underlying soil. The surface heat fluxes (sensible, latent and soil) contain the signature of cellular convection suggesting that the exchange at the ground surface is driven by atmospheric demand. Also notice that the soil temperature and moisture at the first model level in the LSM provide evidence of spatially varied drying and warming; at this last time step, the soil has dried considerably since initialization as it began with a horizontally homogeneous distribution of 21.5% volumetric soil moisture. The soil temperature at the first model level has also increased from its initial horizontally homogeneous value of about 309 K. Cases with heterogeneity reveal a similar evolution and pattern but those patterns are dominated by the disparity between *wet* and *dry* soil. Section 6.2 presents results and discussion of the surface fluxes as influenced by the heterogeneity-induced organized motions.

##### *6.1.1.2 The PBL*

For the DP cases, the influence of the varying soil moisture is evident in the flow visualization of vertical velocity and water vapor mixing ratio contours shown in Figures 6.2 and 6.3. These figures show how the presence or absence of soil moisture variation dramatically alters the turbulent motions in the PBL. Over the region of high soil moisture content (*e.g.*,  $x =$

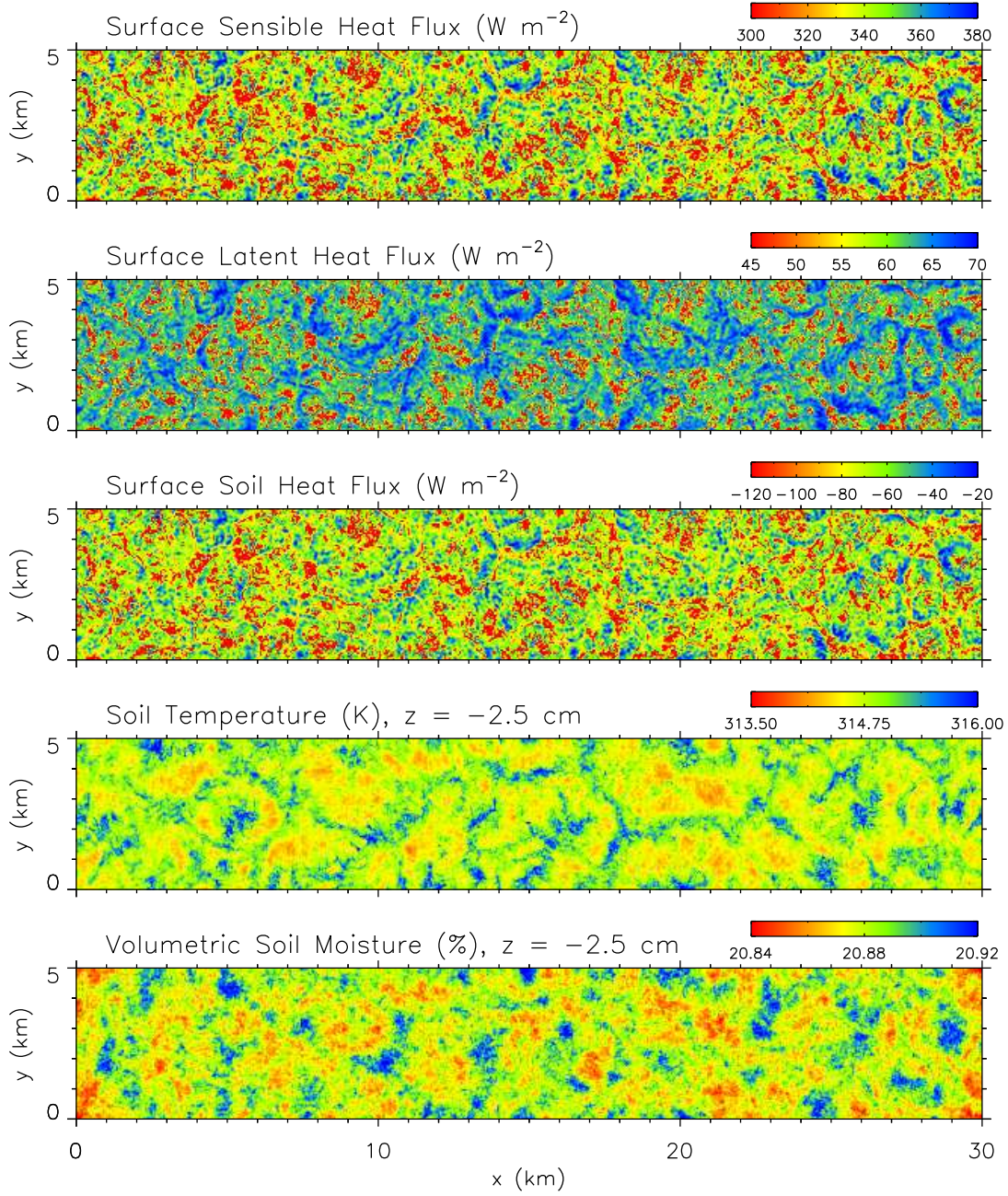


Figure 6.1: Instantaneous  $(x,y)$  slices of surface fluxes (sensible, latent and soil heat fluxes) and the corresponding soil temperature and moisture at the uppermost vertical level in the LSM ( $z = -2.5$  cm, which represents the vertical average over the top five centimeters in the soil) from DP-AS at the last time step in the simulation.



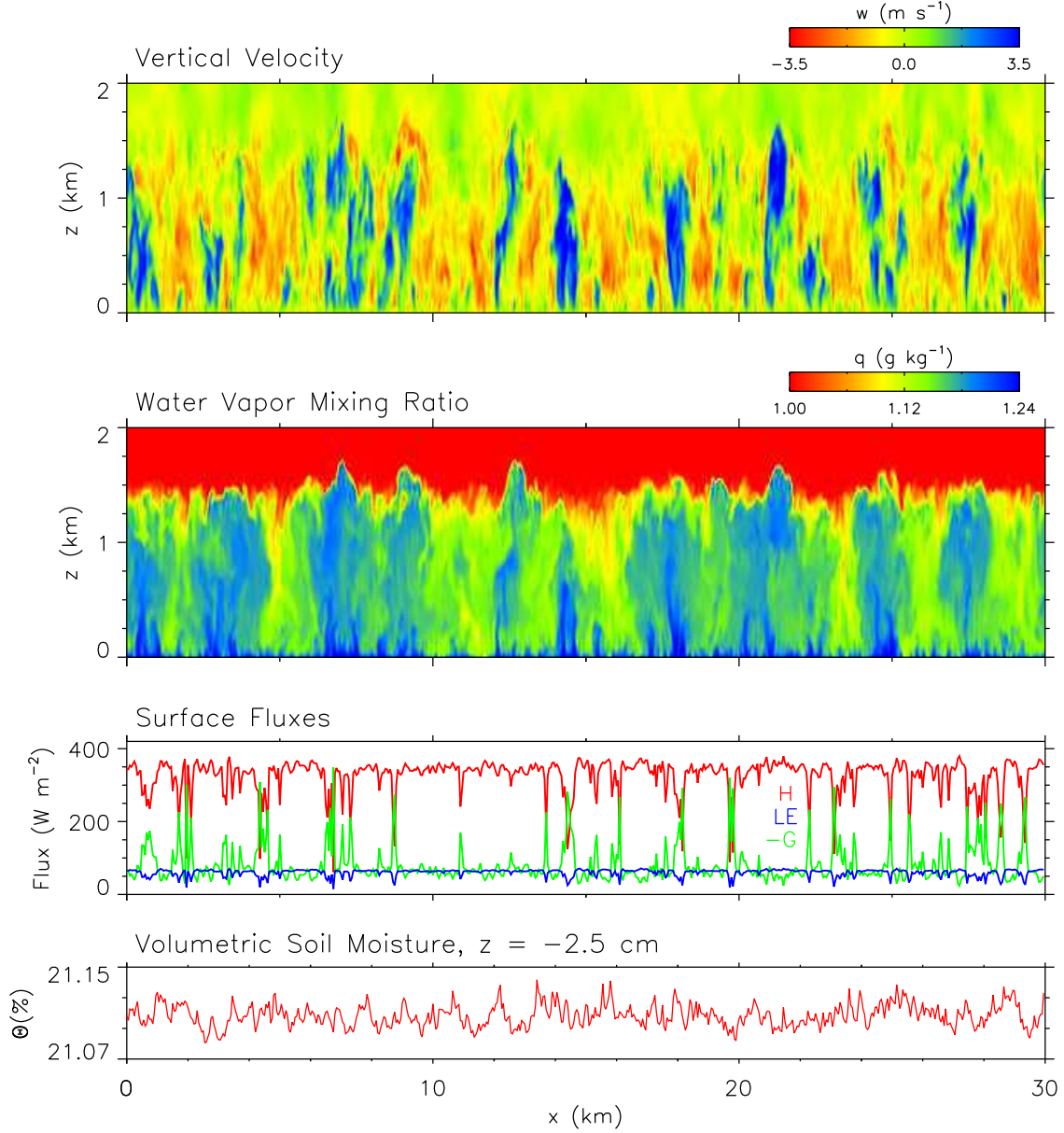


Figure 6.2: Instantaneous two dimensional slices of vertical velocity and water vapor mixing ratio at the first time step used in the averaging for case DP-AS (top two panels). The third panel depicts the coincident surface forcing ( $H$ ,  $LE$ ,  $-G$ ) determined via the LES-LSM coupling. The lowest panel is the volumetric soil moisture at the uppermost soil level,  $z = -2.5$  cm.

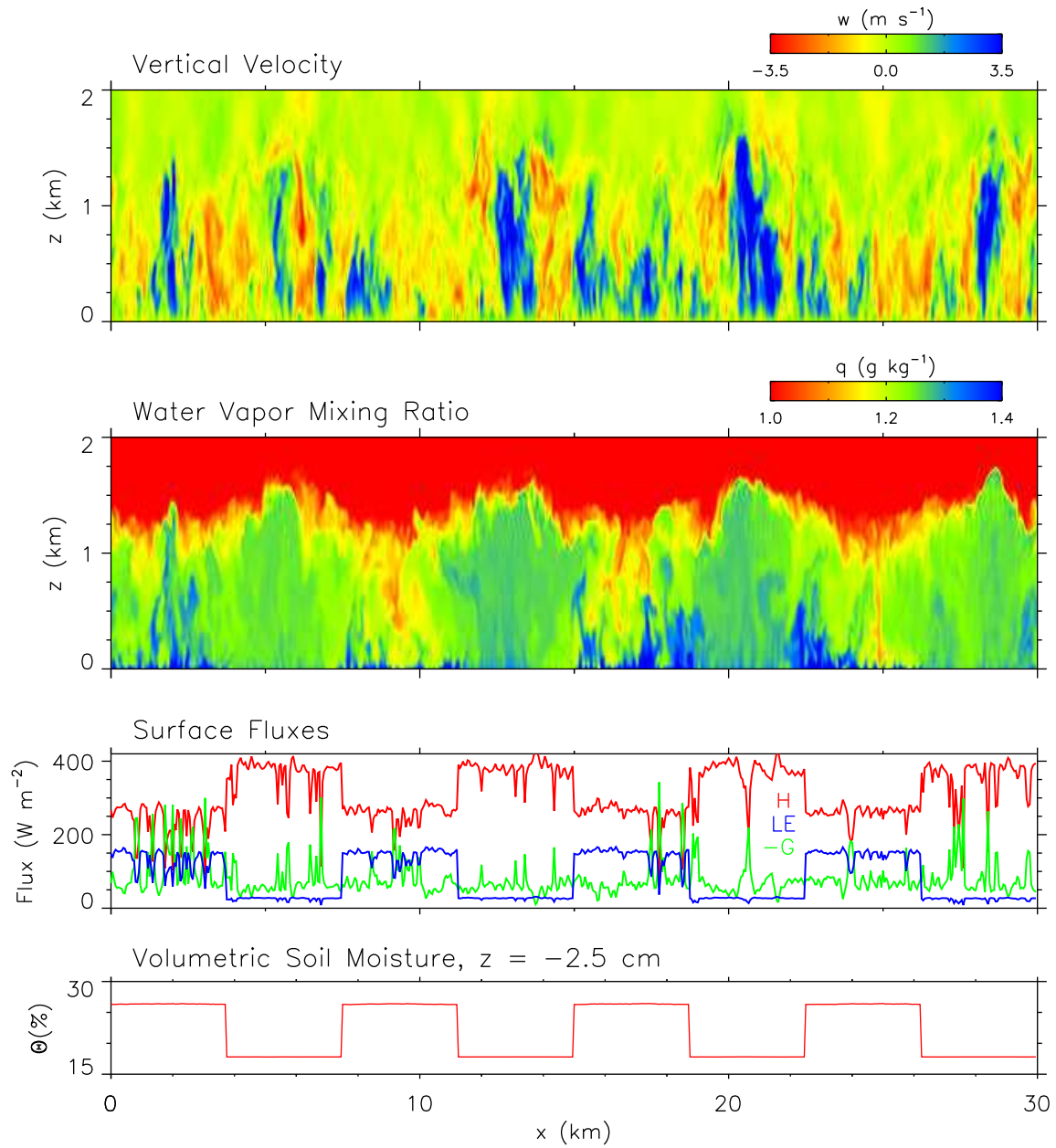


Figure 6.3: The same as Figure 6.2, except for case DP-7.5S.

[0,3.75], [7.5,11.25], [15,18.75], [22.5,26.25] km, Figure 6.3) the convective plumes tend to be less vigorous compared to their counterparts in the region of low soil moisture content.

At the same time, the shape of the PBL interface layer (*i.e.*, the entrainment zone around  $z = 1.3$  to  $1.5$  km) is also altered by soil moisture heterogeneity. Entrainment of low water vapor mixing ratio is observed over the region of high soil moisture and entrained dry air extends all the way to the ground (compare the second panels of Figures 6.2 and 6.3). In general, we see evidence of entrainment of dry air near the plume valleys, similar to that reported by Sullivan et al. (1998). The average normalized mixing ratio in the domain is about the same for the two cases (not shown), but in the DP-7.5S case, averaged vertically, the lowest PBL mixing ratio exists over the soil with the highest volumetric soil moisture; results presented in Section 6.2 will quantify the organized motions responsible for these patterns.

The bottom two panels of Figures 6.2 and 6.3 show the  $x$ -variation of the associated instantaneous surface fluxes and volumetric soil moisture at the uppermost LSM level. In contrast to studies with specified surface fluxes, the fluxes in the current simulations are spatially varying and respond to both the PBL and to soil temperature/moisture. The partitioning of energy by the LSM is evident in both figures, but especially in Figure 6.3 where over the *wet* soil a greater portion of the available energy goes into evaporating water and hence larger latent and smaller sensible heat fluxes compared to that over *dry* soil. Figures 6.2 and 6.3 are presented as examples; the picture is similar for the other heterogeneous cases.

## 6.1.2 Bulk boundary layer statistics

### 6.1.2.1 Surface fluxes

Since the only external input of energy to the simulations is the specified incoming solar radiation, the surface buoyancy forcing  $\theta_{v*}$  is dynamically determined through the LES-LSM coupling. Therefore, it is prudent to quantify the bulk forcing on the PBL. To do so, the horizontally- and time-averaged sensible heat flux ( $H$ ), latent heat flux ( $LE$ ) and the Bowen ratio ( $\beta = H/LE$ ) are calculated. These quantities are presented in Table 4.1. Note that  $\theta_*$  and  $\Theta_*$  can be calculated from  $H$  and  $LE$ , and can be combined into  $\theta_{v*}$ , the surface virtual temperature flux using  $\theta_{v*} = \theta_* + (0.61\theta_o\Theta_*)$ , where  $\theta_o$  is a reference potential temperature.  $\theta_{v*}$  is used throughout the manuscript as the scaling parameter for virtual potential temperature. Table 4.1 also includes the horizontally- and time-averaged

boundary layer heights ( $z_i$ ) and the convective velocity ( $w_*$ ). Here,  $z_i$  is determined by finding the local height of the largest gradient in virtual potential temperature profile at every  $(x, y)$  location and averaging across all  $x$  and  $y$ . This method to determine  $z_i$  was first described as the gradient method in Sullivan et al. (1998), and further described as a wavelet method of minimum dilation in Davis et al. (2000).

As expected, the horizontally homogeneous *dry* soil cases (DS) partition 7.5-7.7 times more incoming solar radiation into sensible heat compared to latent heat than does the *wet* soil case (WS). Also apparent from Table 4.1 is that our attempt to pick soil conditions for the *average* (AS) cases that resulted in average surface fluxes equal to the average of the WS and DS cases was not completely successful, *e.g.*,  $\theta_{v*}$  of the AS cases is larger than the average of those of WS and DS. Nonetheless, we can still use these AS cases as a point of reference. Scaling parameters  $z_i$  and  $w_*$  reveal the expected influence of the magnitude of the surface buoyancy forcing  $\theta_{v*}$ ; the larger  $\theta_{v*}$ , the larger are  $z_i$  and  $w_*$ . Worth noting is that the land-surface model responds as expected to the moisture-state of the PBL; when the PBL is of higher average mixing ratio there is less atmospheric demand for moisture at the ground which is reflected in lower evaporative fluxes in the WP cases compared to the DP cases.

### 6.1.2.2 Surface exchange coefficients

As mentioned earlier, at every  $(x, y)$  location in the domain the surface fluxes of momentum, heat and moisture in these simulations are internally determined through a coupling between a partitioning of the available energy via the SEB and a drag law. The efficiency of the transfer between the land-surface and the PBL is determined by drag coefficients ( $C_m$ ,  $C_h$ ) which are dynamically calculated from surface similarity theory assumed valid locally between the ground and the first LES grid level (which due to the staggered vertical grid system in the LES is 10 m for the  $u, v$ -velocities). Again, we assume that the exchange coefficient for moisture is the same as that for heat.

On average, small-scale land-surface heterogeneity ( $\lambda/z_i \sim 1-2$ ) increases the exchange coefficients for momentum and heat (Figure 6.4), while larger-scale heterogeneity ( $\lambda/z_i \sim 4-9$ ) tends to reduce these exchange coefficients. For flows encountering even larger-scale heterogeneity ( $\lambda/z_i \sim 17$ ), the coefficients decrease compared to  $\lambda/z_i \sim 4-9$  heterogeneity and are tending back toward the values determined from the homogeneous cases.  $C_m$  and  $C_h$  for the  $\lambda/z_i \sim 4-9$  cases are about 6% and 9% lower compared to the AS cases. It is understood that  $C_m$  and  $C_h$  are wind speed dependent (Schlichting, 1979; Brutsaert, 1982;

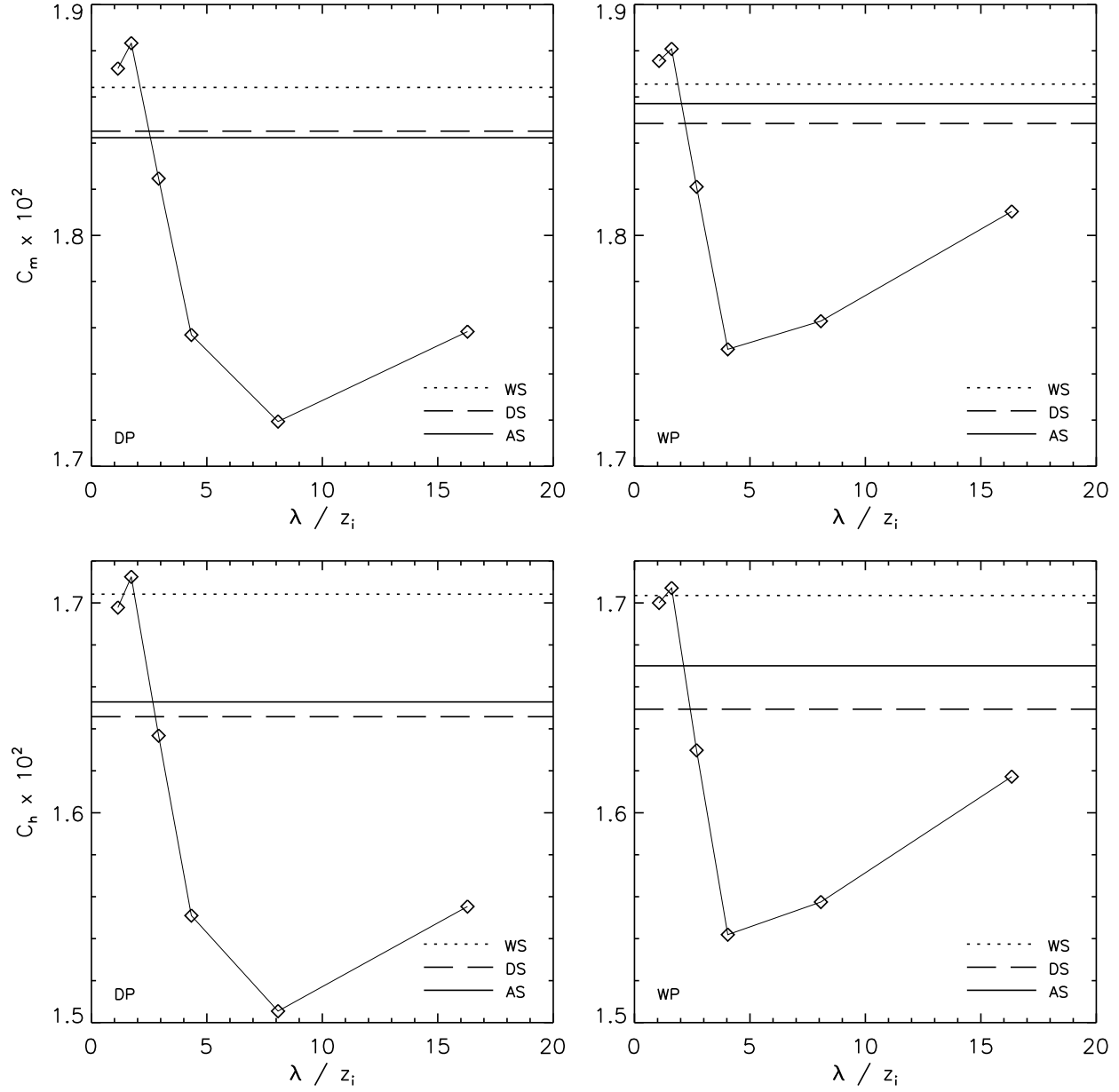


Figure 6.4: Variation of the horizontally- and time-averaged surface exchange coefficients for momentum and heat ( $C_m$  and  $C_h$ ) versus the normalized heterogeneity wavelength ( $\lambda/z_i$ ) for both the DP and WP cases. The line with symbols represents the heterogeneous soil cases. The solid, dashed and dotted lines with no symbols are the homogeneous soil cases.

Mahrt et al., 2001b), and that they decrease with increasing wind speed. The organized motions that develop as a result of the heterogeneity (see Section 6.2), are most intense for the  $\lambda/z_i \sim 4-9$  cases. Therefore, the decrease in  $C_m$  and  $C_h$  for these cases likely results from a persistent increase in surface winds associated with the organized motions.

Comparing the left and right panels of Figure 6.4, there is little or no influence of the initial PBL water vapor mixing ratio on the efficiency of the surface exchange which is consistent with Schlichting's (1979) dimensional analysis suggesting that  $C_m$  should only be a function of Reynold's number\*. While the  $\lambda/z_i \sim 4-9$  cases show the smallest  $C_m$  and  $C_h$ , their surface fluxes of heat and moisture are larger than the others (Table 4.1). This indicates that the gradients of heat and moisture between the ground surface and the first model level are larger on average for these cases than for the other heterogeneous soil cases. This increased gradient manifests itself through slightly lower average soil temperatures and volumetric moisture content combined with slightly higher PBL temperatures and water vapor mixing ratios (not shown). Although the effects are relatively small, this analysis implies greater transfer of heat and moisture from the soil to the PBL in the presence of  $\lambda/z_i \sim 4-9$  scale heterogeneity.

### 6.1.2.3 *Turbulence kinetic energy*

Total turbulence kinetic energy (averaged over the PBL and time,  $\langle \rangle_{PBL,t}$ ) responds to land-surface heterogeneity (Figure 6.5). Heterogeneity at scales larger than 3 km increases the volume- and time-averaged turbulent kinetic energy. The increase in turbulence kinetic energy is due to the generation of organized motions (discussed in Section 6.2). Hadfield et al. (1991) also discussed circulations such as these in their LES simulations, but suggested that the circulation is weak since it only accounts for  $\approx 1\%$  of the kinetic energy in the PBL. The Hadfield et al. (1991) study, however, only looked at two wavelengths of heterogeneity,  $\lambda = (1.5, 4.5)$  km, both of which fall at the small-scale end of this study and are in agreement with these results. As the scale of the heterogeneity increases towards a wavelength of 15 km, the circulation becomes stronger, and then decreases again at even larger scales. The TKE is most affected for cases DP-15S and WP-15S ( $\lambda/z_i \sim 9$ ) which reveal an increase of (14, 19)% respectively compared to the horizontally homogeneous cases.

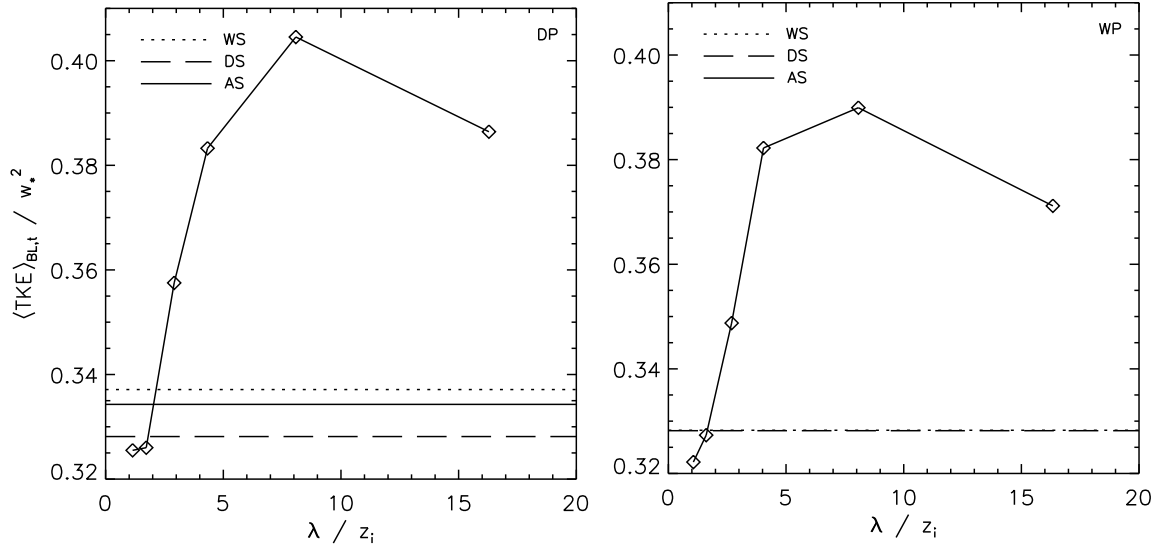


Figure 6.5: Boundary-layer and time averaged turbulence kinetic energy normalized by  $w_*^2$  versus the normalized heterogeneity wavelength ( $\lambda/z_i$ ) for both the DP and WP cases. The line with symbols represents the heterogeneous soil cases. The solid, dashed and dotted lines with no symbols are the homogeneous soil cases.

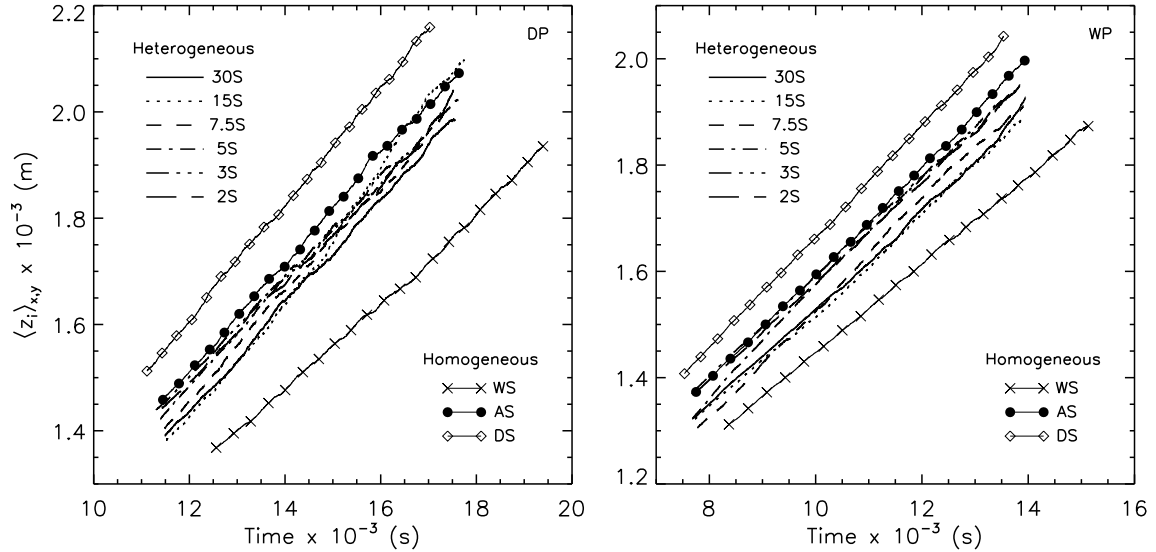


Figure 6.6: Time evolution of the horizontally averaged boundary layer height ( $z_i$ ) for all cases over the complete averaging period for both the DP and WP cases. Lines by themselves represent heterogeneous cases. Lines with symbols represent homogeneous cases.

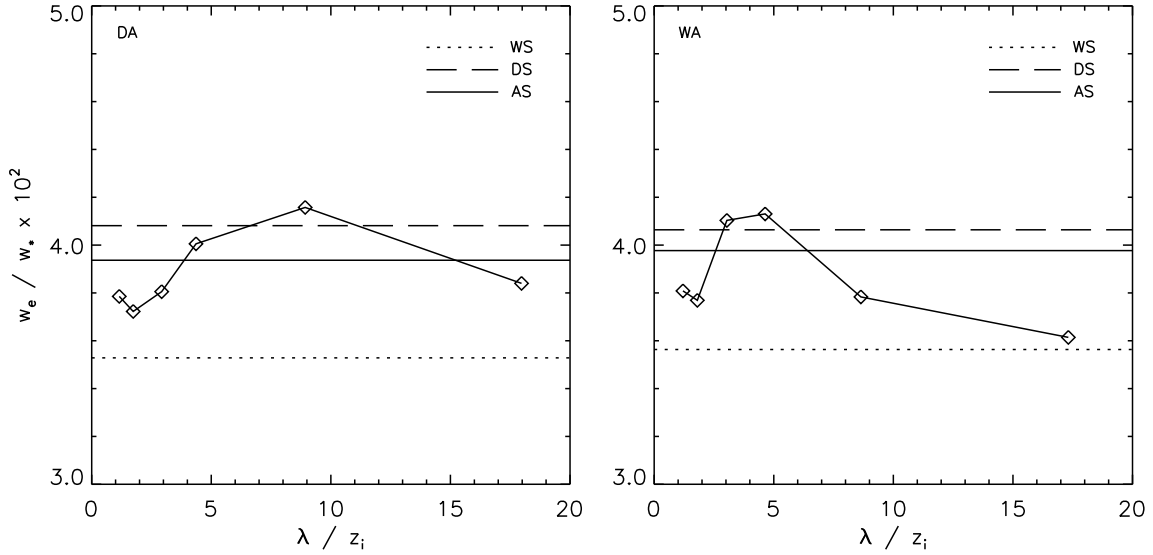


Figure 6.7: Normalized entrainment rates ( $w_e/w_*$ ) versus the normalized heterogeneity wavelength ( $\lambda/z_i$ ) for both the DP and WP cases. The line with symbols represents the heterogeneous soil cases. The solid, dashed and dotted lines with no symbols are the homogeneous soil cases.

#### 6.1.2.4 PBL height and entrainment rates

The growth of the convective layer is tied to the mixing process that occurs at the density interface between the well mixed PBL and the non-turbulent overlying stable layer (Sullivan et al., 1998). Apparent from Figures 6.2 and 6.3, under free convection, heterogeneous soil moisture induces organized PBL motions that alter how the PBL operates. Therefore, it is anticipated that heterogeneity could modify the growth rate of the PBL.

Figure 6.6 depicts the time evolution of the horizontally averaged boundary layer height for all cases. The times presented represent the entire averaging period for our statistics representing (4-9, 8-10) large eddy turnover times ( $z_i/w_*$ ) for the (DP, WP) cases, respectively. The average boundary layer growth is linear with time suggesting that the flow is quasi-steady. All heterogeneous cases fall between the horizontally homogeneous extreme cases (DS and WS).

Entrainment rates ( $w_e = \partial z_i / \partial t$ ) are calculated by performing a least-squares fit to the data presented in Figure 6.6, taking the slope of the fitted line to be  $w_e$ . Heterogeneity and the initial PBL moisture only slightly modify the normalized entrainment rates (Figure 6.7). Heterogeneity-scales on the order of the PBL depth tend to decrease normalized entrainment

---

\*Note that  $C_h$  depends on  $C_m$  (Brutsaert, 1982).



rates compared to the AS cases, although this decrease is only (5.6, 5.5)% for the (DP, WP) cases respectively. Heterogeneity-scales of (9, 5) times  $z_i$  slightly increase the entrainment rates for the (DP, WP) cases, but this increase is only (5.3, 3.8)% compared to the AS cases, respectively. These entrainment rates are also slightly higher than the homogeneous dry soil cases (DS). Even larger heterogeneity ( $\lambda/z_i \sim 18$ ) tends to slightly decrease entrainment rates. These results are counter to Avissar and Schmidt's (1998) comments that heterogeneously-induced organized motions dramatically increase the rate at which the PBL entrains. However, they made these comments without actually calculating  $w_e/w_*$ . Similar rates of entrainment are found for the homogeneous cases when comparing dry versus wet PBLs (compare the left and right panels of Figure 6.7). For both homogeneously- and heterogeneously-forced PBLs, the normalized entrainment rates presented in Figure 6.7 are noticeably higher ( $\sim 0.04$ ) than those presented in Sullivan et al. (1998) ( $\sim 0.02$ ) due to both the relatively weak inversion and to the strong surface forcing in these simulations compared to those in Sullivan et al. (1998).

The combined results presented in Figures 6.5 and 6.7 indicates that the entrainment rate is not directly proportional to TKE, rather entrainment appears more dependent on the rate of heating. We can only make this statement as it applies to free convective PBLs interacting with and in equilibrium with strip-like heterogeneity.

### 6.1.3 Horizontally averaged statistics

#### 6.1.3.1 Velocity variances

The moisture state of the PBL does not vastly influence horizontal and vertical velocity variances (Figures 6.8 and 6.9). Compared to the horizontally homogeneous cases,  $\langle u''^2 \rangle / w_*^2$  near the ground and entrainment zone follows a natural progression (increase, peak, and decrease) when transitioning from small-scale (2 km,  $\lambda/z_i \sim 1$ ) to large-scale (30 km,  $\lambda/z_i \sim 18$ ) heterogeneity (Figure 6.8). Lateral variances ( $\langle v''^2 \rangle / w_*^2$ ) are quite similar for all cases (not shown).

The increase in horizontal velocity fluctuations, at both the ground and  $z_i$ , is consistent with the presence of 2-D organized circulations induced by the strip-like heterogeneity. Hadfield et al. (1991) and Avissar and Schmidt (1998) both showed velocity fluctuations to increase at these locations in the presence of heterogeneity. However, Hadfield et al.'s (1991) largest heterogeneity scale ( $\lambda/z_i$ ) was about 4 and they were therefore unable to trace the pattern back towards homogeneity with increasing  $\lambda/z_i$  as depicted in Figure 6.8. Avissar

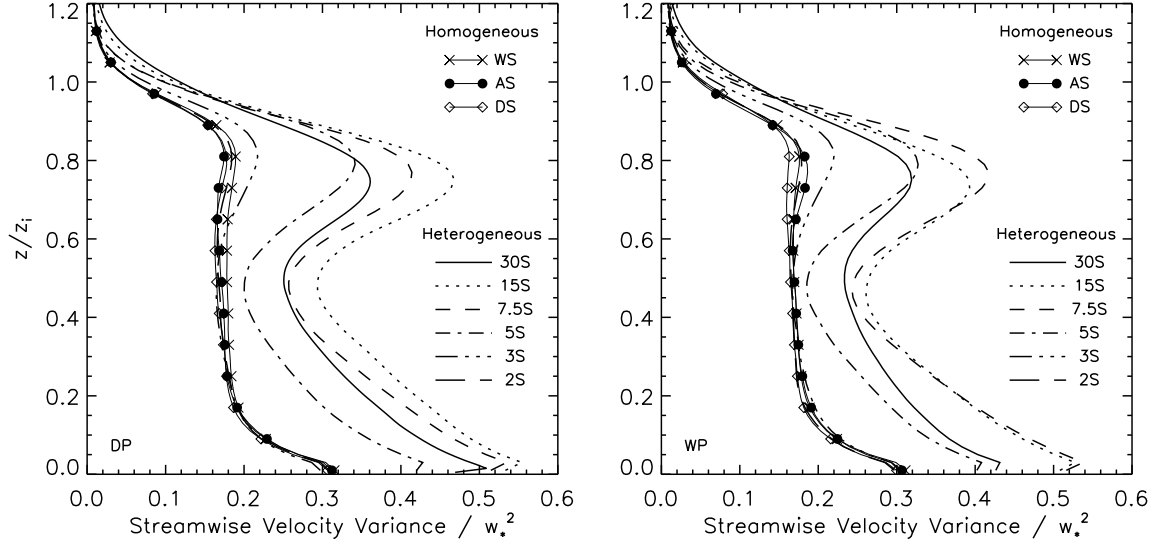


Figure 6.8: Vertical profiles of normalized horizontal velocity variance,  $(\langle u'^2 \rangle + \frac{2}{3} \langle e \rangle) / w_*^2$ , for both the DP and WP cases. Lines by themselves represent heterogeneous cases. Lines with symbols represent homogeneous cases. The variable  $e$  is the subgrid-scale energy as predicted by the LES.

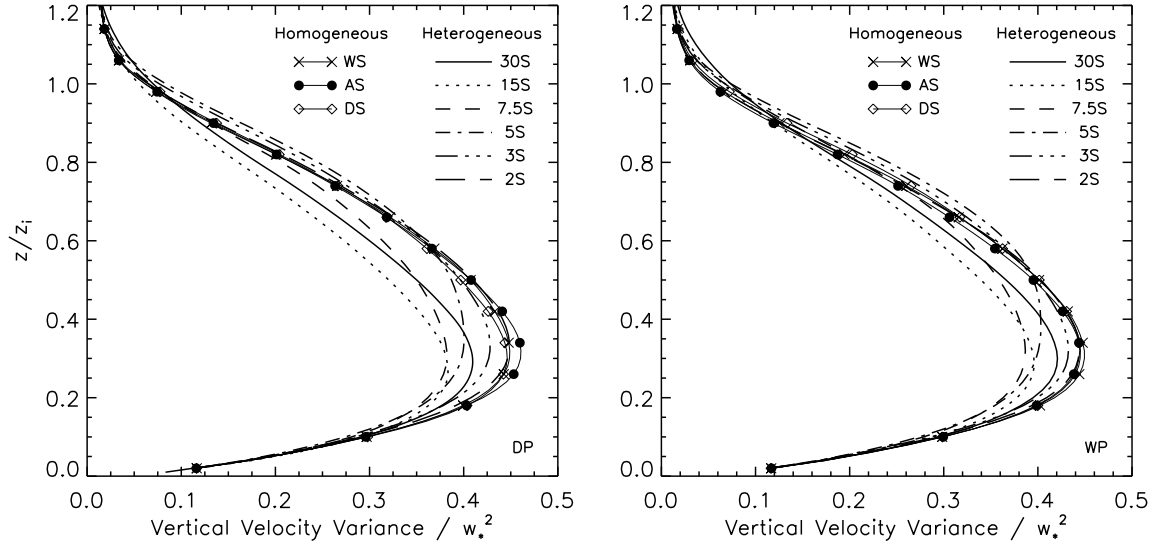


Figure 6.9: Vertical profiles of normalized vertical velocity variance,  $(\langle w'^2 \rangle + \frac{2}{3} \langle e \rangle) / w_*^2$ , for both the DP and WP cases. Lines by themselves represent heterogeneous cases. Lines with symbols represent homogeneous cases.

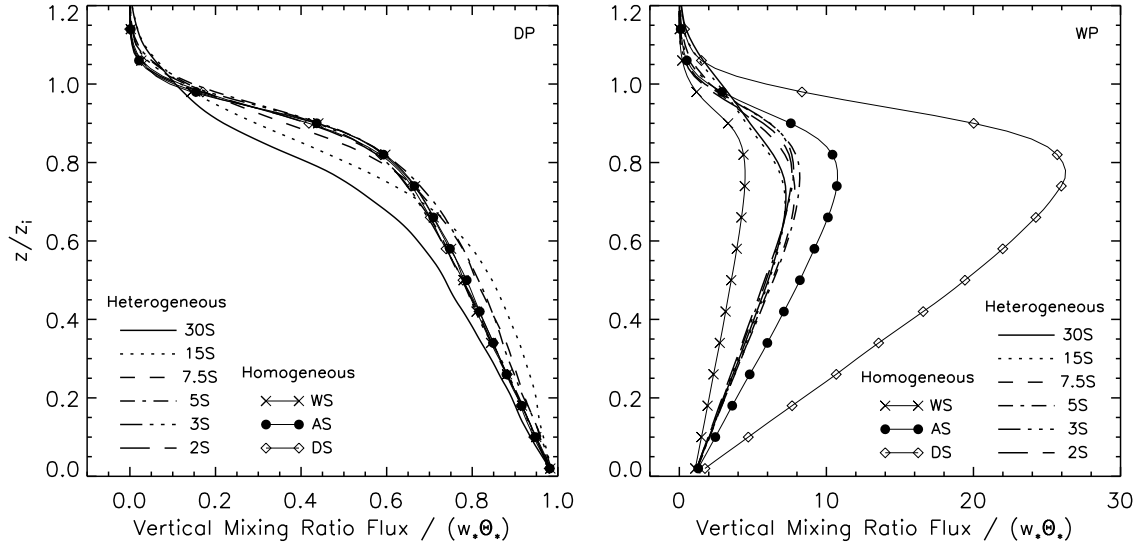


Figure 6.10: Vertical profiles of normalized vertical flux of water vapor mixing ratio ( $\langle w''q'' + \tau_{wq} \rangle / (w_* \Theta_*)$ ) for both the DP and WP cases. Lines by themselves represent heterogeneous cases. Lines with symbols represent homogeneous cases.  $\tau_{wq}$  is the subgrid-scale vertical mixing ratio flux predicted by the subgrid-scale model.

and Schmidt's (1998) results, however, suggested that for this surface heat flux across the patches ( $\sim 0.1 \text{ m K s}^{-1}$ ) the fluctuations should trace the pattern like that in Figure 6.8.

With the exception of the increase of  $\langle u''^2 \rangle / w_*^2$  near  $z_i$ , the response of the velocity variances to heterogeneity (Figures 6.8 and 6.9) is strikingly similar to the expected change between shear- and buoyancy-driven PBLs. Moeng and Sullivan (1994) showed  $\langle u''^2 \rangle / w_*^2$  to increase appreciably near the ground in the presence of a mean velocity shear. They also showed  $\langle w''^2 \rangle / w_*^2$  to decrease in the mid-PBL for increasing shear. Therefore at least with respect to velocity variances, these free convective PBLs in the presence of land-surface heterogeneity are somewhat analogous to free convective PBLs over homogeneous surfaces but with a mixed shear-buoyant forcing.

### 6.1.3.2 Vertical scalar flux

For the DP PBLs, profiles of normalized vertical mixing ratio flux show only a small influence of surface heterogeneity (left panel, Figure 6.10). WP cases also show little influence of heterogeneity (right panel, Figure 6.10), but the horizontally homogeneous cases reveal the influence of the soil partitioning of the available solar energy. As discussed in Section 6.1.2.1, case WP-DS partitions less available energy into latent heat and therefore more energy goes

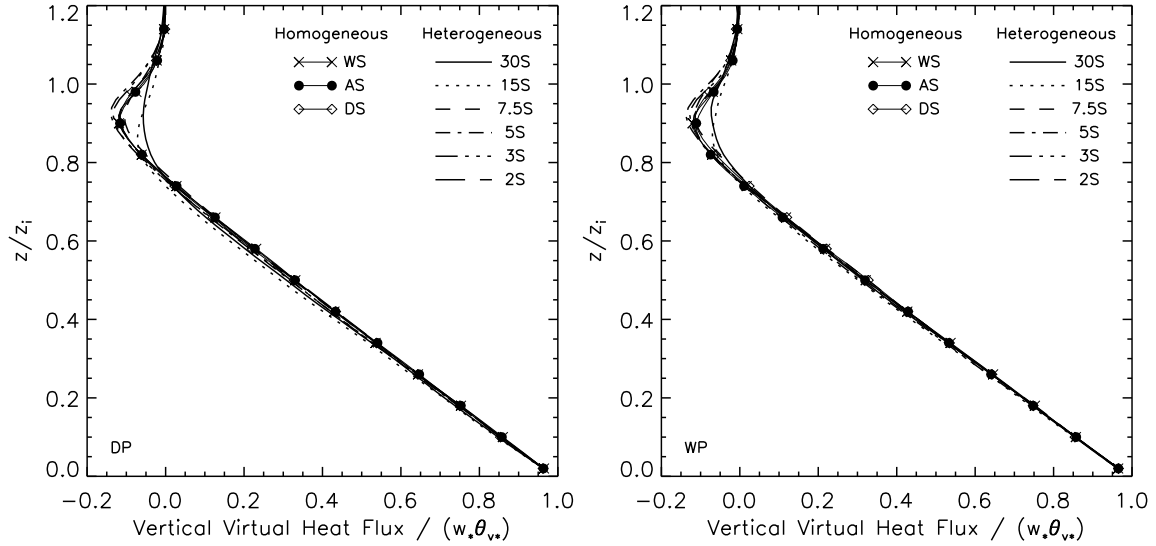


Figure 6.11: Vertical profiles of normalized vertical flux of virtual potential temperature ( $\langle w''\theta_v'' + \tau_w\theta_v \rangle / (w_*\theta_{v*})$ ) for both the DP and WP cases. Lines by themselves represent heterogeneous cases. Lines with symbols represent homogeneous cases.  $\tau_w\theta_v$  is the subgrid-scale vertical virtual potential temperature flux predicted by the subgrid-scale model.

into sensible heat. Case WP-DS also entrains nearly three times more dry air than does WP-AS due to the much larger moisture jump across  $z_i$ .

Normalized profiles of vertical virtual potential temperature flux are linear through the PBL suggesting that our averaging is sufficient to assume quasi-steady conditions (Figure 6.11). These results are counter to earlier findings (Avisar and Schmidt, 1998) who suggested that vertical potential temperature flux profiles are dramatically modified by heterogeneity. The profiles reveal very little modification due to land-surface heterogeneity no matter if the PBL is initially dry or wet (Figure 6.11). These results are consistent with the entrainment rate calculations presented in Figure 6.7, and suggest that the moisture component is truly not passive. In all cases, the profiles have a minimum flux (just below  $z_i$ ) to surface flux ratio of about -0.12 which is smaller than the traditional value of -0.2 (Deardorff, 1979). According to Lilly (2002), this smaller minimum flux to surface flux ratio results from horizontal averaging across an undulating interface.

## 6.2 Phase-averaged fields

### 6.2.1 Definition of averaging procedures and nomenclature

In the free convective PBL ( $-z_i/L_o^\dagger \rightarrow \infty$ ), coherent organized structures are largely responsible for the transport of atmospheric constituents (*e.g.*, Schmidt and Schumann, 1989). Different stability regimes (ranges of  $z_i/L_o$ ) tend to produce varying types of organized motions (Moeng and Sullivan, 1994; Glendening, 1996; Lin et al., 1996; Khanna and Brasseur, 1998). Heterogeneous surface forcing also produces organized motions (Hechtel et al., 1990; Hadfield et al., 1991; Shen and Leclerc, 1995; Avissar and Schmidt, 1998; Albertson and Parlange, 1999; Raasch and Harbusch, 2001; Esau and Lyons, 2002). Of interest here is how organized motions induced through heterogeneous surface forcing alter the mechanics of turbulent transport compared to coherent structures in a homogeneously forced PBL.

A method to identify organized motions induced by the surface heterogeneity is to partition a particular variable into its ensemble averaged, phase-correlated, and background turbulence components (*e.g.*, Hussain and Reynolds, 1970; Sullivan et al., 2000). In this method, we decompose any random signal  $f$  into

$$f(x, y, z, t) = \langle f \rangle(z) + f_p(x, z) + f'(x, y, z, t) \quad (6.1)$$

where  $\langle f \rangle(z)$ ,  $f_p(x, z)$ ,  $f'(x, y, z, t)$  are the ensemble average, phase-correlated, and background turbulence variables, respectively.  $\langle f \rangle(z)$  results from averaging over all  $(x, y, t)$  and  $f_p(x, z) = \tilde{f}(x, z) - \langle f \rangle(z)$  where  $\tilde{f}(x, z)$  is defined as an average over  $(y, t)$  and also periodically imaged in  $x$  with length  $\lambda$ . Thus,  $f_p(x, z)$  represents the average deviation from the ensemble mean at a particular  $(x, z)$  location<sup>‡</sup>. In presenting statistics,  $x$ -averages of phase-correlated variables are needed and this operation is denoted by  $[\ ]$ . For a single variable,  $[f_p] = 0$  by construction and thus we often show the  $x$ -average of the absolute value  $[|f_p|]$ . We emphasize that  $x$ -averages of phase products, for example the vertical flux  $[w_p f_p]$  or variance  $[f_p^2]$ , are not equal to zero. The above conditional sampling technique is applied to our suite of simulated PBLs that span a range of heterogeneous surface conditions.

---

<sup>†</sup> $L_o$  is the Obukhov length,  $L_o = -\rho u_*^3 / (k g [\frac{H}{\theta_o C_p} + 0.61E])$ , where  $k$  is the von Kármán constant. The other variables are defined in the Appendices.

<sup>‡</sup>Since the impact of the heterogeneity depends on the length scale of the heterogeneity and on the relative height compared to the PBL depth ( $z_i$ ), the phase-correlated results are presented in a normalized coordinate system  $x/\lambda$  versus  $z/z_i$ .

Unlike Avissar and Schmidt (1998), no subsidence has been imposed in our simulations. Therefore, no attempt is made to force the boundary layer to have similar depth over each side of the heterogeneity. When calculating statistics, the vertical coordinate is first normalized by that time-step's horizontally averaged  $z_i$ , and then quantities are interpolated to a fixed  $z/z_i$  grid prior to time averaging. Consequences of this averaging appear in the phase-averaged fields since for any given heterogeneity-scale, the PBL-top can vary dramatically from the *wet*-side to the *dry*-side. Therefore, near the PBL-top, horizontal averaging in the  $x$ -direction can include regions both inside and outside the PBL. Our averaging is similar to the averaging from airplane flight legs where data are gathered at a fixed height above the ground, and when the PBL top changes along the flight path these averages include regions both above and below the entrainment interface.

## 6.2.2 Influence of varying $\lambda/z_i$ on the land surface

To illustrate the influence of varying patch size ( $\lambda$ ) relative to the PBL depth ( $z_i$ ), we present three cases with  $\lambda = 30$  km, 7.5 km, and 3 km, which correspond to  $\lambda/z_i \sim 18$ , 4, and 1, respectively. Section 6.1 showed that cases with land surface heterogeneity at scales  $4 < \lambda/z_i < 9$  exhibit the most dramatic differences compared to homogeneous cases. They also show that heterogeneous surfaces not only modify the PBL turbulent motions but also the underlying soil properties.

### 6.2.2.1 Soil properties

At the uppermost soil level ( $z = -2.5$  cm) in the case with  $\lambda/z_i \sim 4$  (DP-7.5S, middle left panel of Figure 6.12), phase-correlated soil temperatures show local maxima in the middle of both the *wet* and *dry* patches. Away from the patch centers, phase-correlated temperatures gradually cool toward the patch boundaries. This soil temperature pattern reveals a feedback from the patch-induced organized motions in the PBL. As shown in Section 6.2.3, two-counter rotating cells are induced in the PBL which result in fairly strong horizontal winds above the soil surface at the patch edges but stagnation points at the middle of the patches. These circulations also lead to spatially varying surface heat flux (shown in the next subsection) and hence the soil temperature pattern.

The pattern mentioned above is similar for the  $\lambda/z_i \sim 18$  and 1 (DP-30S and DP-3S) cases, with modest differences. The warming of the upper soil is more evenly distributed across each patch in the  $\lambda/z_i \sim 18$  (DP-30S) case, while the warming response for the case

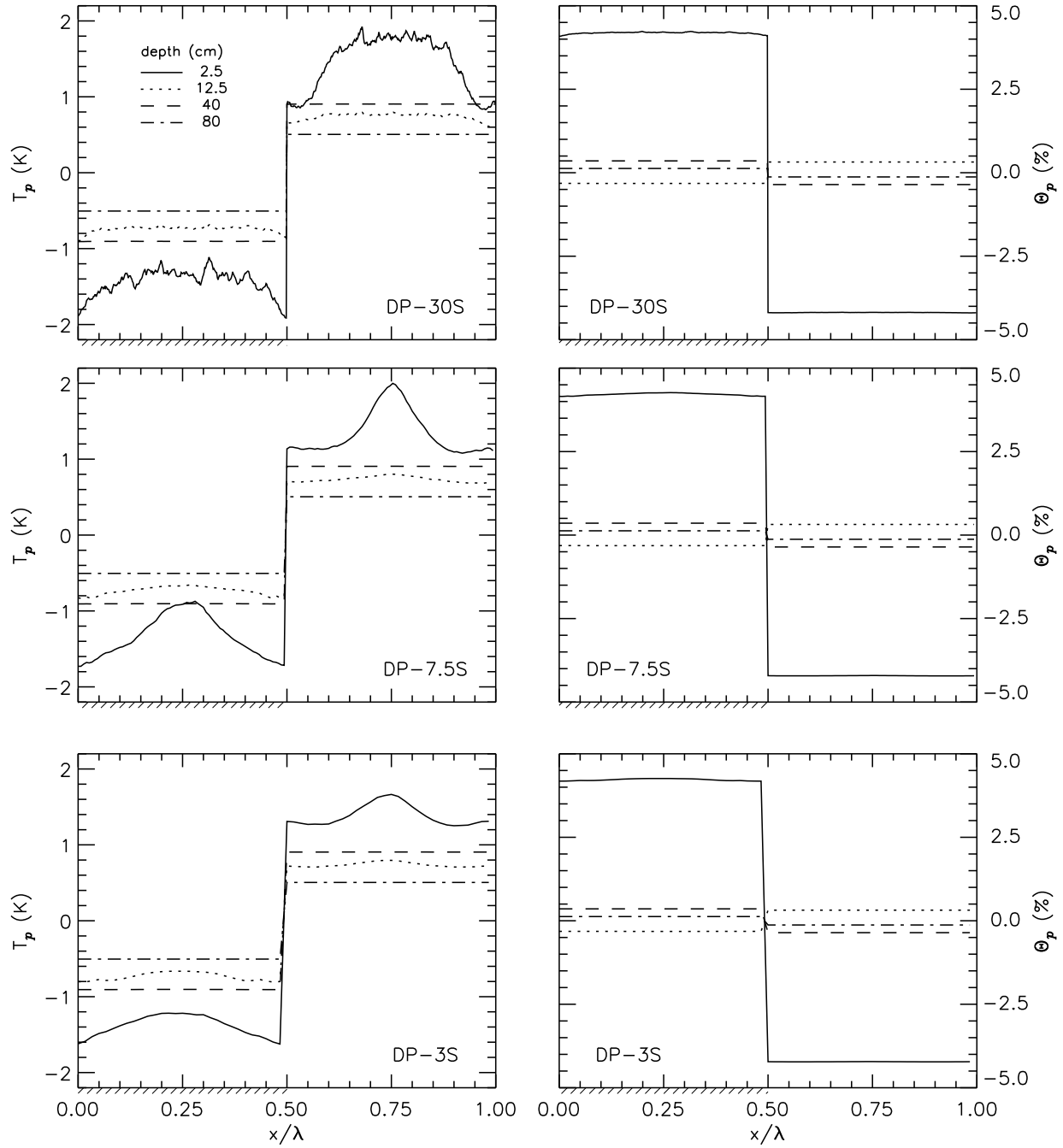


Figure 6.12: The  $x/\lambda$  variation of phase-correlated soil temperature,  $T_p$  (K, left column), and phase-correlated soil moisture,  $\Theta_p$  (% , right column) for cases DP-30S (top row), DP-7.5S (middle row), and DP-3S (bottom row). Each panel presents results at the four soil levels in the LSM (solid:  $z = -2.5$  cm, dotted:  $z = -12.5$  cm, dashed:  $z = -40$  cm, dash-dot:  $z = -80$  cm). The hatches demarcate the  $x/\lambda$  extent of the *wet* soil.

with  $\lambda/z_i \sim 1$  (DP-3S) is only about half that of the case with  $\lambda/z_i \sim 4$  (DP-7.5S). These variations arise from distinct differences in the organized motions that develop due to the heterogeneity, as discussed in detail in Section 6.2.3.

Detailed inspection of the phase-correlated soil moisture shows that it has a similar variation to the phase-correlated soil temperature (the large dynamic range of  $\Theta_p$  prevents showing small scale fluctuations in Figure 6.12).  $\Theta_p$  varies little with heterogeneity scale ( $\lambda/z_i$ ). Opposite to predictions from a linearized model (Brubaker and Entekhabi, 1996), the *wet* patch is more influenced by heterogeneity-induced winds than is the *dry* patch. Brubaker and Entekhabi's (1996) analytic model suggests that both soil temperature and moisture are more sensitive to wind speed fluctuations when the soil is dry. These differences are likely attributed to our LSM which accounts for nonlinear coupling between soil temperature, moisture, surface fluxes and the overlying wind.

The response of soil temperature and moisture to heterogeneity-induced organized motions is similar between the DP and WP cases (not shown). This lack of response to a significant overall increase in atmospheric water vapor ( $\Delta q \sim 7 \text{ g kg}^{-1}$ ) confirms Brubaker and Entekhabi's (1996) finding that  $q$  is a small player in determining the soil moisture and temperature state.

### 6.2.2.2 Surface fluxes

The phase-correlated surface fluxes, depicted in Figure 6.13, show the impact of the organized motions on the coupling between the atmosphere and the land-surface. Over the *wet* soil (left panels), for all but the  $\lambda/z_i \sim 1$  case (dashed curves), the phase-correlated fluxes are a minimum in the center of the patch. As shown in Figure 6.14 this corresponds to the foot of the descending branch of the patch-induced circulation so the near-surface phase-averaged horizontal velocity is nearly zero at this location. This leads to minimum surface fluxes at this location. On the other hand, the  $\lambda/z_i \sim 1$  case (dashed curves) exhibits little variation across the *wet* patch, or even slight flux increases near the center of the patch (especially the soil heat flux  $G_p$ ). Although a stagnation point of the patch-induced circulation still exists at the center of the patch in this smaller  $\lambda/z_i$  case, the magnitude of the organized circulation is much weaker than the background turbulent wind field. A similar trend is seen in the WP cases (not shown), although the variations are seen more in the sensible and soil heat fluxes as expected since the atmosphere demands less water in this case compared to the DP cases.

Over the *dry* soil (right column, Figure 6.13), the phase-correlated surface heat fluxes are



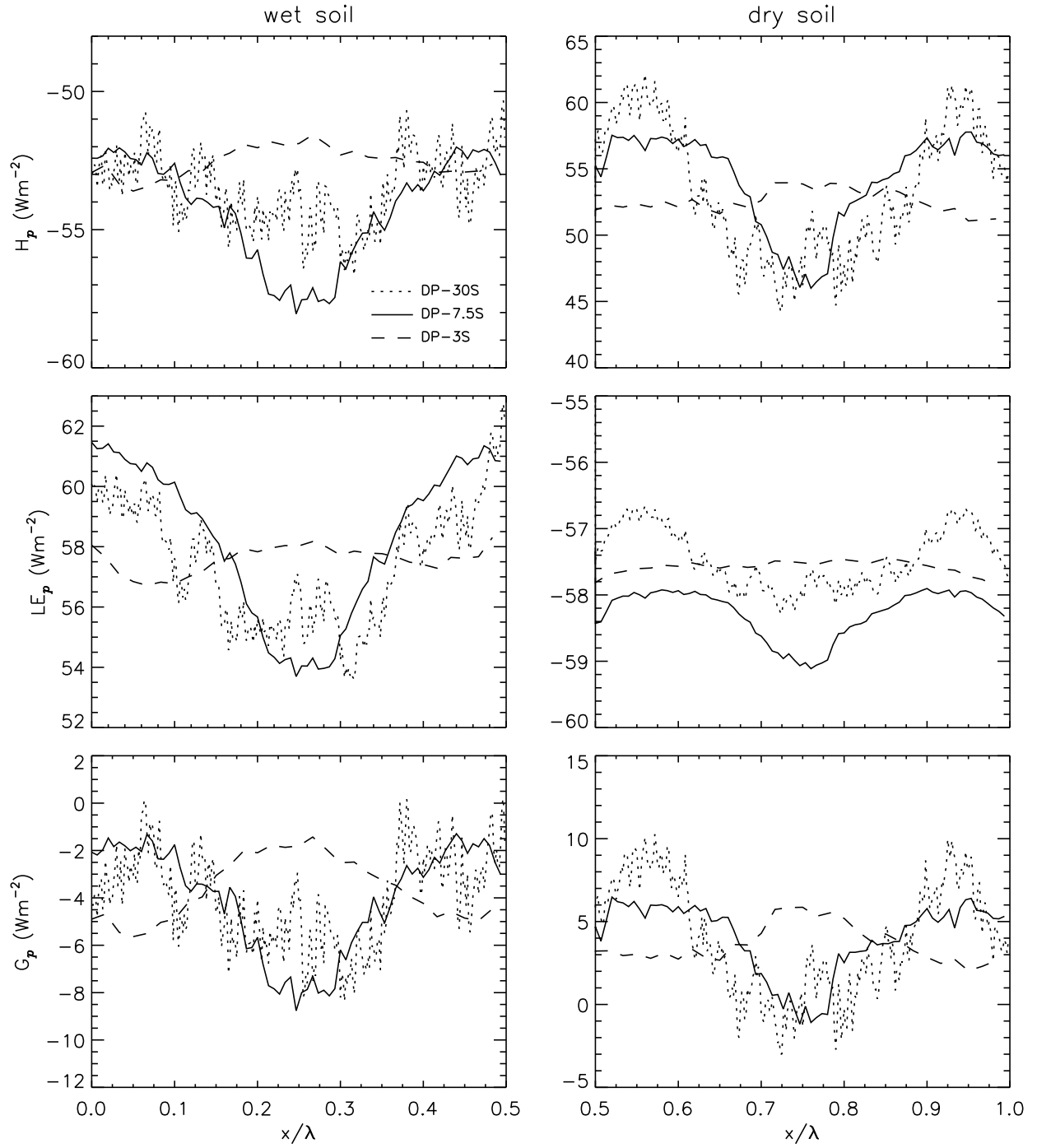


Figure 6.13: Phase-correlated sensible ( $H_p$ ), latent ( $LE_p$ ), and soil ( $G_p$ ) surface heat fluxes over the *wet* soil (left) and *dry* soil (right) for cases DP-30S (dotted)  $\lambda/z_i = 18$ , DP-7.5S (solid)  $\lambda/z_i = 4$  and DP-3S (dashed)  $\lambda/z_i = 1$ .

again minimized at the center of the patch. But the fluxes on the *dry* side peak at about  $x/\lambda = 0.6$  and  $0.9$ , instead of at the edges of the patch at on the *wet* side. The location of these maxima suggests that the peak in phase-correlated horizontal velocities are skewed toward the center of the patch (see Figure 6.14). It is important to note that the organized motions created in simulations with imposed surface forcing, such as those presented in Avissar and Schmidt (1998), would not exhibit this same behavior since in their study the thermal gradient induced by the forcing is fixed in space and time.

### 6.2.3 Influence of varying $\lambda/z_i$ on heterogeneity-induced PBL fields

#### 6.2.3.1 Velocity

For case DP-7.5S ( $\lambda/z_i \sim 4$ ), the phase-correlated vertical motions (middle right panel of Figure 6.14) are most intense over the central core of the *dry* soil ( $x/\lambda \sim 0.75$ ) with weaker sinking motion elsewhere. The rising motion is confined to 25% of the wavelength of the heterogeneity centered about the middle of the *dry* patch. Based on the  $(u_p, w_p)$  flow fields, we envision the organized flow pattern to consist of two counter-rotating cells of oblong shape. The cells coincide over the center of the *dry*-patch to form what appears to be a single bubble of rising motion. Near the ground, the fluid speed increases as air over the *wet* soil is brought towards the region of rising motion, but is deflected upwards before the stagnation point of horizontal velocity centered over the *dry*-soil. The air approaching from both sides rapidly rises over the *dry*-patch in a narrow core, subsequently being deflected outwards by the inversion, and decreases in speed as it leaves the upwelling region. The return leg consists of weaker momentum fluid closing the return leg over a much broader area, but again centered over the *wet* patch. This picture is similar to the schematic presented by Segal and Arritt (1992) when discussing velocity patterns associated with mesoscale circulations.

The upper and lower panels of Figure 6.14 show that the intensity of these circulations varies with the scale of the heterogeneity. In addition, these figures show that in cases with large heterogeneity, *e.g.*, DP-30S ( $\lambda/z_i \sim 18$ ), individual plumes (on a scale of  $1-2 z_i$ , much smaller than the patch size) can develop near the center of both the *wet* and *dry* patches, away from the edge of the heterogeneity.

#### 6.2.3.2 Virtual temperature and moisture

Two-dimensional plots of phase-correlated scalar fields illustrate the influence of the heterogeneity-induced organized dynamics on PBL scalar transport (Figure 6.15). For the case with  $\lambda/z_i \sim$

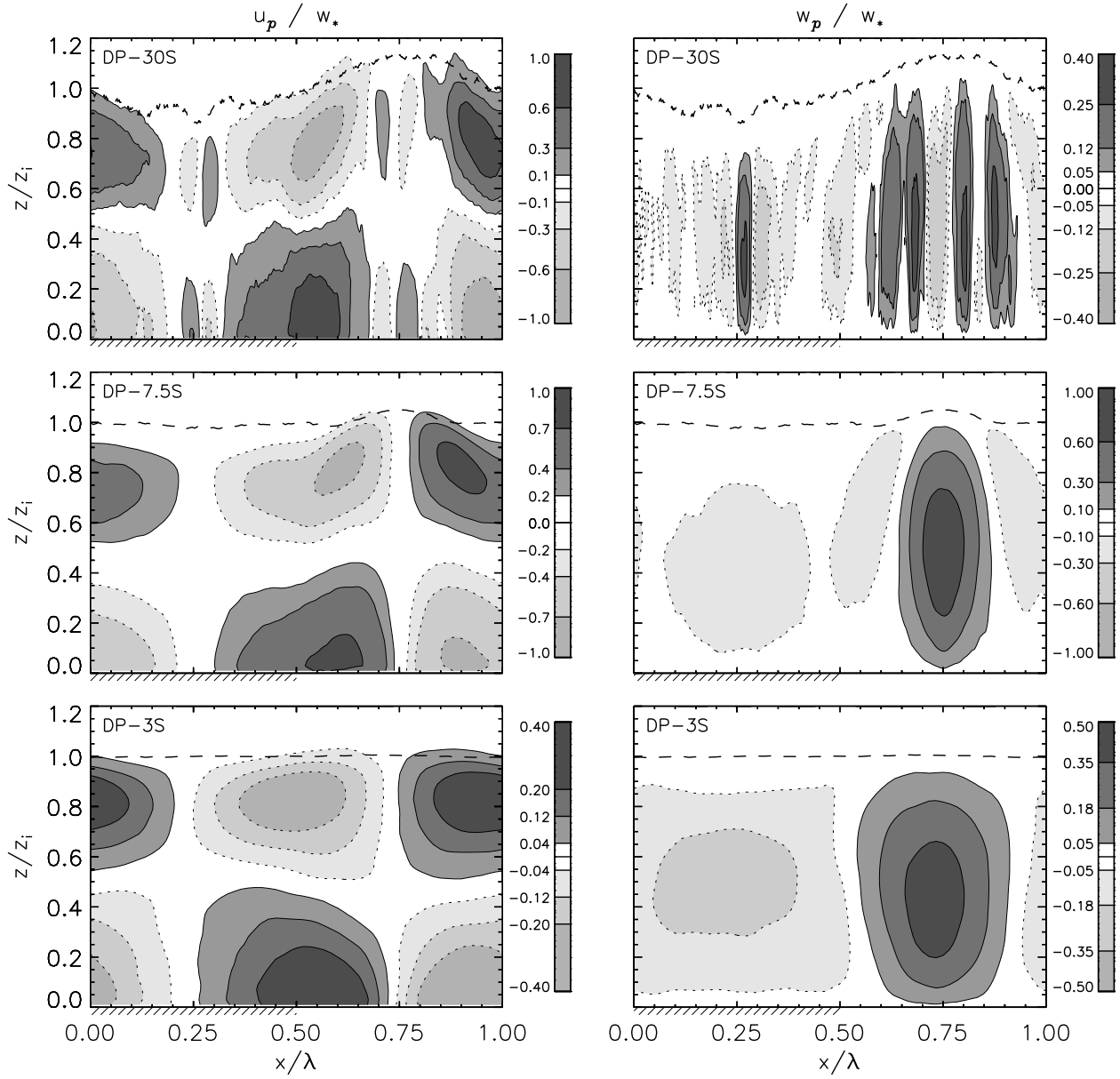


Figure 6.14: Normalized phase-correlated horizontal velocity ( $u_p/w_*$ , left column) and vertical velocity ( $w_p/w_*$ , right column) as a function of  $x/\lambda$  and  $z/z_i$  for cases DP-30S (top), DP-7.5S (middle), and DP-3S (bottom). The dashed-line is the phase-averaged boundary layer depth,  $z_{i_p}$ ; dotted contours represent negative phase-correlated values; and the hatches demarcate the  $x/\lambda$  extent of the wet soil.

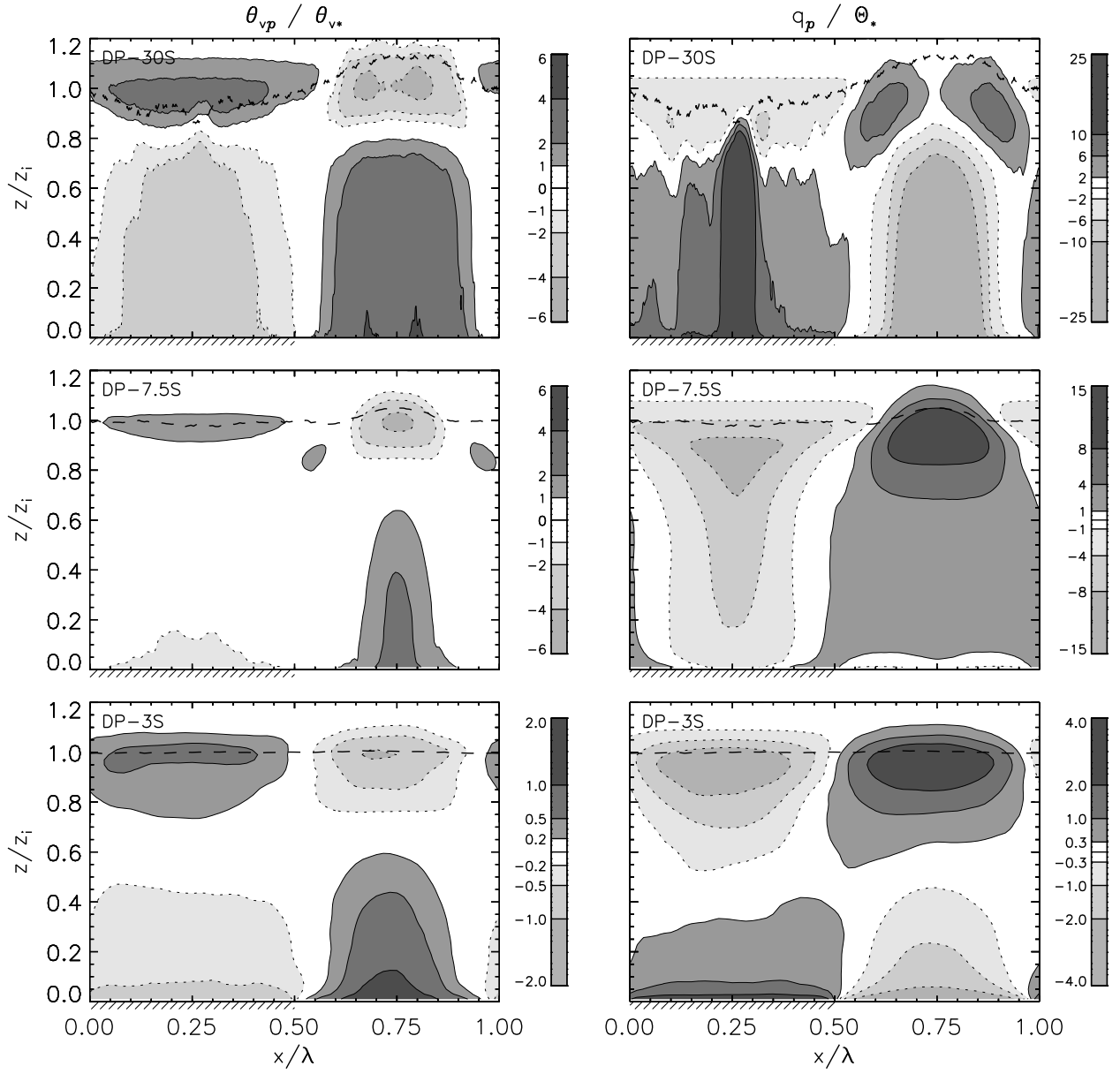


Figure 6.15: Normalized phase-correlated virtual potential temperature ( $\theta_{vp}/\theta_{v*}$ , left column) and water vapor mixing ratio ( $q_p/\Theta_*$ , right column) as a function of  $x/\lambda$  and  $z/z_i$  for cases DP-30S (top row), DP-7.5S (middle row), and DP-3S (bottom row). All markings on the figures are the same as those defined in Figure 6.14. Note the change in magnitude for the different cases.

4 (DP-7.5S), the phase-correlated potential temperature reveals relatively cool air near the *wet* surface and relatively warm air over the *dry* surface in the lower PBL. The opposite is true near the entrainment zone, with relatively cool air at the top of the rising motion, lobes of relatively warm air at either side and generally warm air near the descending portions of the organized motions. Sullivan et al. (1998) suggested that in the absence of velocity shear, entrainment does not occur at the center of plumes but rather at the plume edges. The middle left column of Figure 6.15 is consistent with this view; at the top of the plume, the contours of potential temperature are lifted up becoming tightly packed preventing entrainment of the overlying air mass, but at the plume edges and along the upper return path of the organized cell, warm air is entrained from aloft.

The middle right panel of Figure 6.15 shows organized motion advecting tongues of high mixing ratio air from over the *wet* soil to regions over the *dry* soil near the surface, and entrainment of dry air from aloft being brought down over the *wet* soil for case DP-7.5S. This leads to a wetter PBL over the *dry* patch than that over the *wet* patch, which is confirmed in flow visualizations on an instantaneous basis (shown in Section 6.1.1). This feature is present in cases with  $4 < \lambda/z_i < 9$  which exhibit the most intense heterogeneity-induced organized circulations. In the  $\lambda/z_i \sim 18$  case (DP-30S), the opposite is true where over the *wet* (*dry*) patch the PBL is relatively wet (dry). In the  $\lambda/z_i \sim 1$  case (DP-3S), the PBL layer-averaged moisture is about the same on both sides of the heterogeneity and also averages to be about zero as in the homogeneous cases.

Comparison of the left and right columns of Figure 6.15 suggests that the phase-averaged contours of potential temperature are clearly distinct from those of water vapor mixing ratio, and hence the organized transport of active and passive scalars tends to be different. The water vapor field response varies more with changing  $\lambda/z_i$  than does the virtual potential temperature field.

Also in the left panels of Figure 6.15, we observe that the normalized spatial distribution of the phase-induced virtual potential temperature (*i.e.*, contours plotted in  $x/\lambda$  and  $z/z_i$  variables) varies only modestly with the heterogeneity scale ( $\lambda/z_i$ ). However, over the bulk of the PBL the magnitude of  $\theta_{vp}/\theta_{v*}$  increases continuously with increasing  $\lambda/z_i$ . Not unexpectedly, patch-induced water vapor mixing ratio also increases with  $\lambda/z_i$  (compare the right three panels in Figure 6.15), but responds directly to the patch-induced velocity field as expected for a passive scalar. Figure 6.14 reveals that plumes persist near the center of each patch in case DP-30S. In the top right panel of Figure 6.15, a narrow region of excessive moist air (with a mixing ratio of 10-20 non-dimensional water vapor mixing ratio

units) centered over  $x/\lambda = 0.25$  suggests the presence of moist air over this region is largely unaware of the dry atmosphere located about 15 km away. No such narrow region of cold air is visible in the virtual potential temperature field, indicating that passive and active scalars mix differently in these simulations.

### 6.2.3.3 Fluxes of virtual temperature and moisture

The phase-induced vertical fluxes of temperature and water vapor are a consequence of the coherence between  $(w_p, \theta_{vp})$  and  $(w_p, q_p)$  over the depth of the PBL. In the left panel of Figure 6.16, we observe that the maximum virtual potential temperature flux induced by the organized motions is located near the center of the *dry* patch where the organized circulation has the strongest updraft (right panels of Figure 6.14). These fluxes peak in the middle of the PBL and turn negative above  $z/z_i \sim 0.8$  as relatively cool air penetrates into the warm inversion. Weak positive potential temperature fluxes persist over a localized portion of the *wet* soil ( $0.2 < x/\lambda < 0.3$ ), where cold boundary-layer air recirculates back down over the *wet* soil region. The flux in the  $\lambda/z_i \sim 18$  (DP-30S) case behaves differently than in the other cases because of the formation of smaller-than-patch-size plumes near the centers of both *dry* and *wet* patches, as shown in the velocity field.

Phase-correlated vertical mixing ratio fluxes are also maximized at the center of the updraft core in DP-7.5S ( $\lambda/z_i \sim 4$ ) (right middle panel, Figure 6.16) where the organized circulation effectively transports moist air upward. This positive moisture flux peaks at about  $z/z_i = 0.85$  rather than in mid-PBL like the phase-correlated virtual potential temperature fluxes. At the top of the PBL immediately away from the rising core where the flow encounters the inversion, deflects outward, and begins to descend, two small regions of negative vertical phase-correlated mixing ratio flux are present. In these regions  $w_p < 0$  and  $q_p > 0$ , and is a signature of moist air being brought down (re-circulated back) in these regions, not dry air entrained from the inversion. The positive moisture flux over the *wet* soil, however, indicates drier air (presumably mixed with entrained dry air from inversion) is brought down over the *wet* soil region.

The above picture is supported by the variation of horizontal flux of the phase-correlated fields. The variation of  $u_p \theta_{vp}$  (left panels of Figure 6.17) shows cool air being transported from the center of the *wet* soil region towards the *dry* land, but on reaching the edge of the *dry* patch, the horizontal flux becomes positive because of mixing with warm air from the *dry* land. Convergence of horizontal flux is readily apparent at the center of the *dry* patch where the vertical flux due to the organized motion is maximized (Figure 6.14). Aloft, relatively

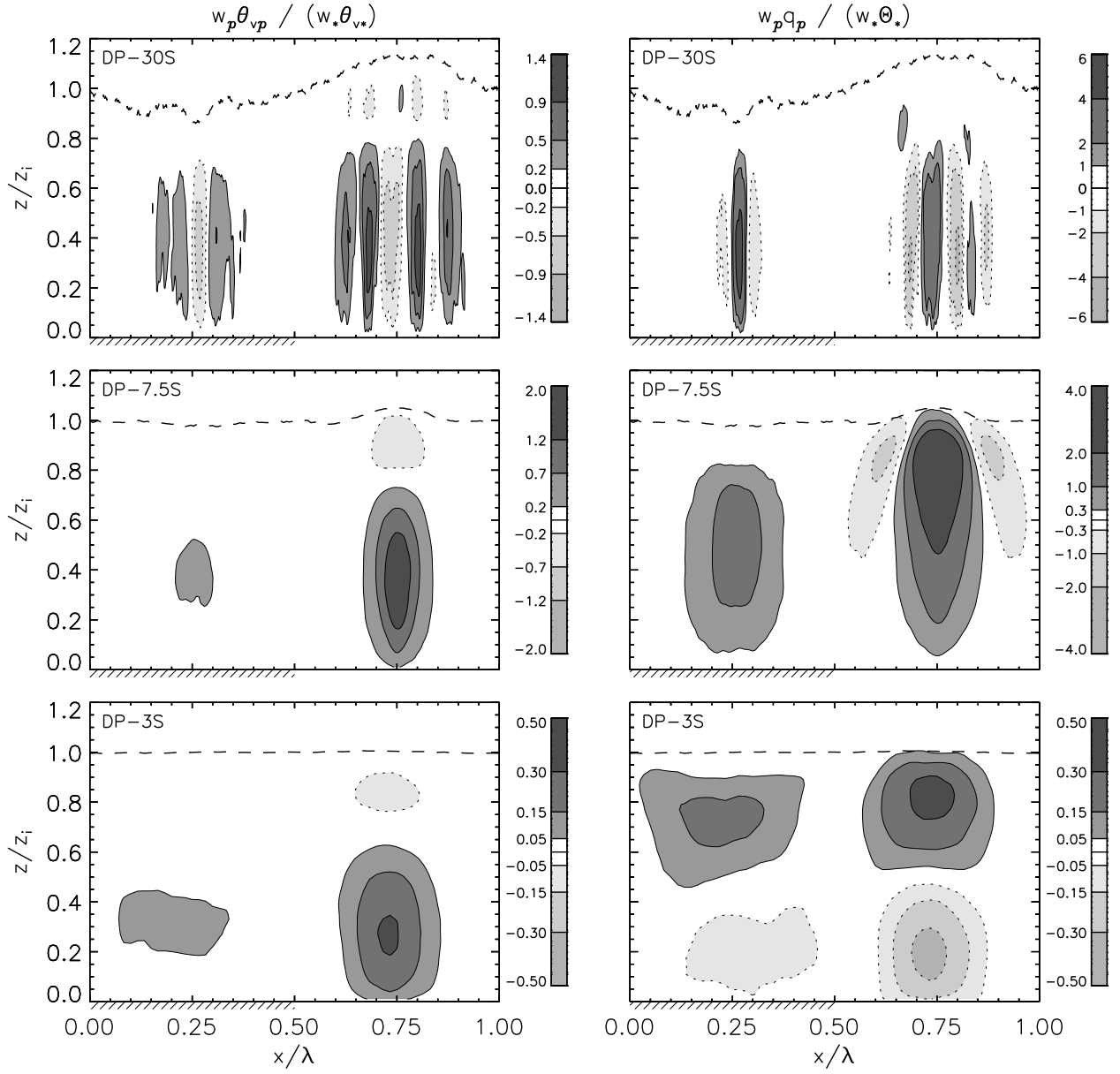


Figure 6.16: Normalized phase-correlated vertical virtual potential temperature fluxes,  $w_p \theta_{vp} / (w_* \theta_{v*})$  (left column) and vertical water vapor mixing ratio flux,  $w_p q_p / (w_* \Theta_*)$  (right column) as a function of  $x/\lambda$  and  $z/z_i$  for cases DP-30S (top), DP-7.5S (middle), and DP-3S (bottom). All markings on the figures are the same as those defined in Figure 6.14.

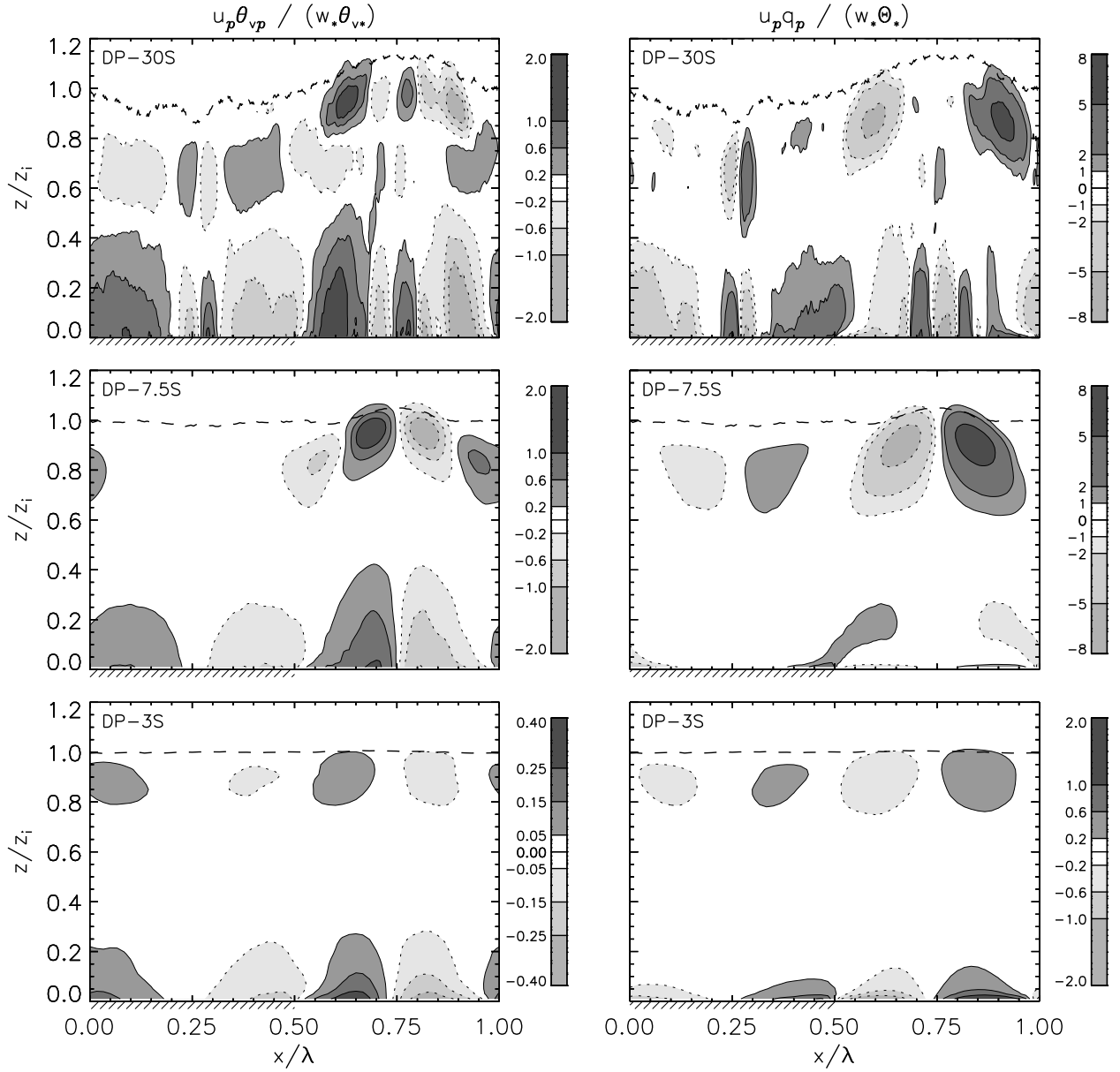


Figure 6.17: Normalized phase-correlated horizontal virtual potential temperature fluxes,  $u_p \theta_{vp} / (w_* \theta_{v*})$  (left column), and horizontal water vapor mixing ratio fluxes,  $u_p q_p / (w_* \Theta_*)$  (right column), as a function of  $x/\lambda$  and  $z/z_i$  for cases DP-30S (top), DP-7.5S (middle), and DP-3S (bottom). All markings on the figures are the same as those defined in Figure 6.14.



cool air leaves the updraft core, but at the edges of the updraft plume entrained warm air is transported laterally towards the *wet* soil side. Similar patterns appear at all heterogeneity scales, although the signature is more pronounced in the DP-30S case.

Near the ground in case DP-7.5S ( $\lambda/z_i \sim 4$ ), phase-correlated horizontal mixing ratio fluxes show tongues of moisture transported from the *moist* patch to regions over the *dry* patch (right middle panel, Figure 6.17). These tongues are elevated over the relatively dry air persisting immediately over the hot, dry soil. Moist air is laterally transported away from the region near top of the updraft, and relatively dry air entrained from aloft is brought to the center of the downwelling leg of the circulation. In case DP-30S ( $\lambda/z_i \sim 18$ ), these tongues also exist, but only extend to about  $0.05x/\lambda$  into the *dry* patch. Immediately in the center of the *dry* patch in this case, the persistent plumes are again apparent. No such tongues of moist air are present in the DP-3S ( $\lambda/z_i \sim 1$ ) case.

The 2-D phase-correlated dynamical fields from the WP cases are similar to the DP cases, but the influence of the PBL's initial water vapor state is most noticeable in the phase-correlated water vapor mixing ratio and its vertical flux, shown in Fig. 6.18. The magnitude of the peak phase-correlated water vapor mixing ratio is about (9, 15, 18) times larger for cases WP-(30S, 7.5S, 3S), respectively, compared to the DP cases. Compared to the DP cases, the 2-D patterns of  $q_p/\Theta_*$  in the WP cases are similar but the features near the entrainment zone are more pronounced due to the much larger moisture jump  $\Delta q$  across the entrainment interface (see Figure 4.1). The increase in phase-correlated  $q_p/\Theta_*$  for the WP cases results in similar increases in the magnitudes of  $w_p q_p/(w_* \Theta_*)$ .

## 6.2.4 Profiles of $x$ -averaged phase-correlated fields

### 6.2.4.1 Velocity

Figure 6.19 compares the phase-correlated horizontal and vertical velocity variances for all heterogeneous cases. The influence of heterogeneity does not vary linearly as  $\lambda/z_i$  varies from 1 to 18. Optimum scales of surface heterogeneity to generate significant patch-induced motion are  $4 < \lambda/z_i < 9$ . For  $4 < \lambda/z_i < 9$ ,  $[u_p^2]$  increases by about a factor of nine compared to the homogeneous cases while  $[w_p^2]$  increases by nearly a factor of four at  $\lambda/z_i \sim 3$ . Meanwhile, at scales  $\lambda/z_i > 9$  and  $\lambda/z_i < 3$  the magnitudes of  $([u_p^2], [w_p^2])/w_*^2$  approach zero. In other words there appears to be an optimum scale of heterogeneity  $\lambda/z_i$  between 4 and 9 that generates the most intense organized motions. Roy and Avissar (2000) suggested that heterogeneous surface forcing induces a horizontal pressure gradient and if that force is

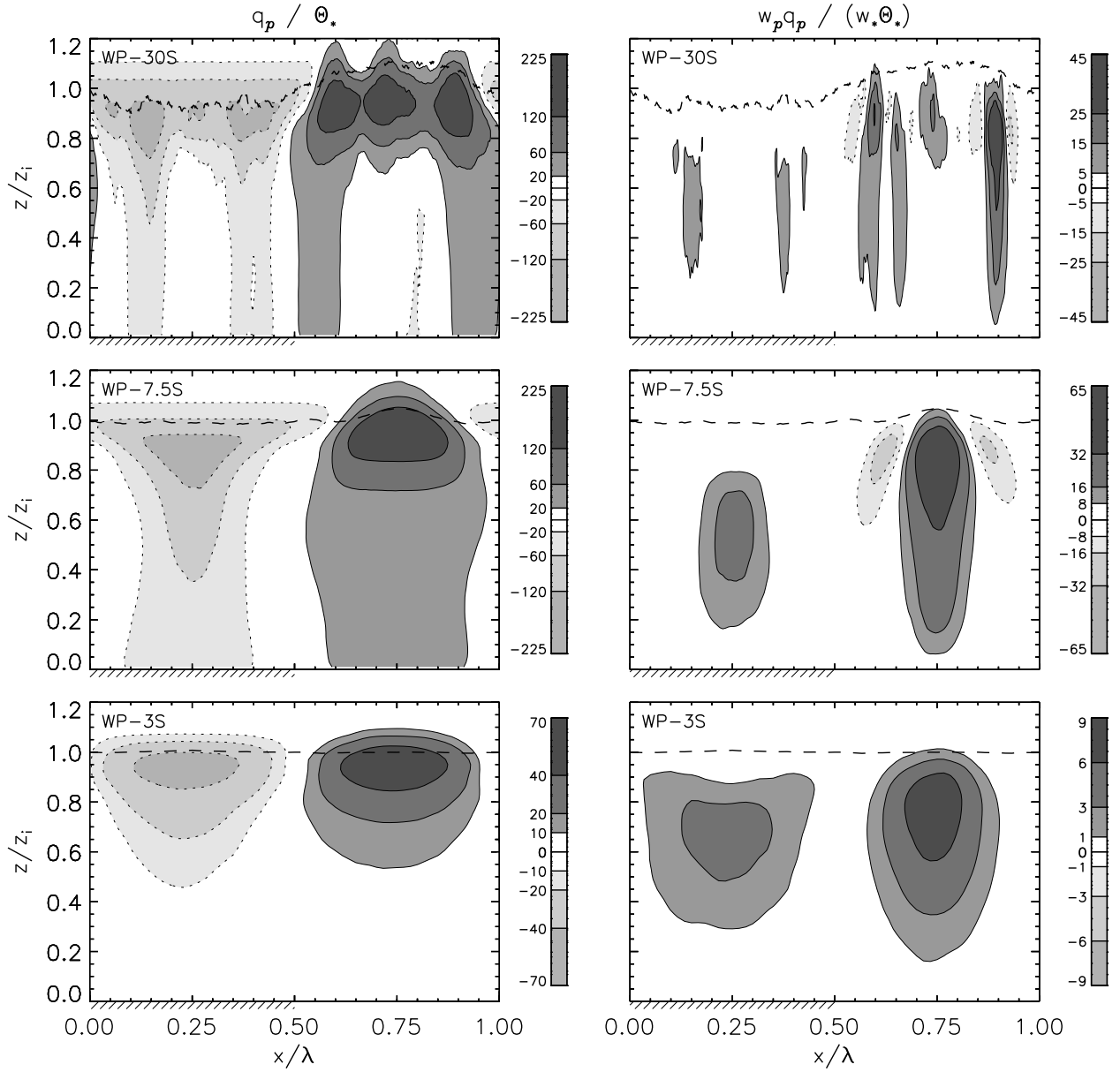


Figure 6.18: Normalized phase-correlated water vapor mixing ratio,  $q_p/\Theta_*$  (left column) and phase-correlated vertical water vapor mixing ratio flux,  $w_p q_p/(w_* \Theta_*)$  (right column) as a function of  $x/\lambda$  and  $z/z_i$  for cases WP-30S (top), WP-7.5S (middle), and WP-3S (bottom). All markings on the figures are the same as those defined in Figure 6.14.

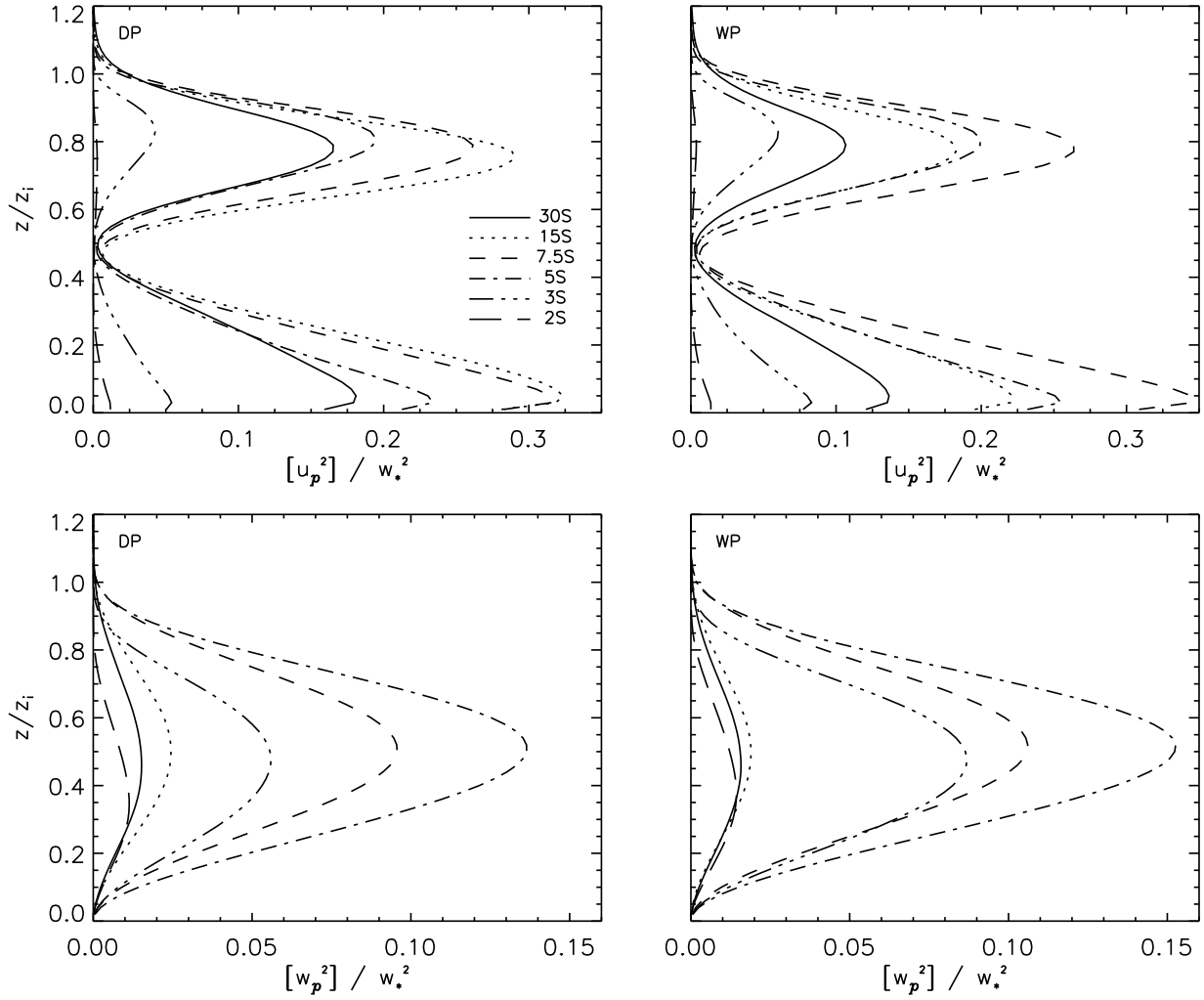


Figure 6.19: The normalized  $x$ -average of the square of the phase-correlated horizontal velocity ( $[u_p^2]/w_*^2$ ) and vertical velocity ( $[w_p^2]/w_*^2$ ) for all cases with heterogeneity. The left hand panels depict DP cases and the right hand panels WP cases.

larger than the buoyant forcing, the atmosphere is dominated by the “rolls” induced by the heterogeneity. If the balance switches such that the buoyant forcing dominates the pressure gradient, then the rolls are typically broken down into small-scale plumes, which may explain the features seen in our cases with small  $\lambda/z_i$ . Comparing the right and left panels of Figure 6.19 shows no significant effect on the patch-induced velocity variances due to the moisture content in the PBL (i.e., between DP and WP cases).

#### 6.2.4.2 Scalars

The variation of the patch-induced scalar fields exhibit a marked difference compared to the velocity fields. Figure 6.20 shows the vertical profiles of the standard deviations of virtual potential temperature and water vapor mixing ratio fluctuations for all heterogeneous cases; in general the intensity of scalar fluctuations increases with increasing patch size (note that  $\theta_{v*}$  and  $\Theta_*$  are about the same among different  $\lambda/z_i$  cases, DP or WP, see Table 4.1). The largest heterogeneity (30S) cases show a notably larger magnitude compared to the other heterogeneous cases because small-scale plumes develop in the center of each patch, where relatively cool (wet) air remains over the relatively cool (wet) soil and the warm (dry) air remains over the relatively warm (dry) soil without much mixing of the two distinct air masses. Near the PBL top, both virtual potential temperature and water vapor mixing ratio show the largest patch-induced scalar variation likely due to patch-induced  $z_i$  variation between dry-soil and wet-soil regions. This is particularly noticeable in the 30S cases where near  $z_i$  the phase-correlated scalar fields are either larger or smaller than the horizontal mean values depending on whether its local PBL top is higher or lower than the horizontal mean  $z_i$  (Figure 6.15). Whether the atmosphere is initially *wet* (right panels) or *dry* (left panels) does not significantly change the overall picture of the dependence on patch size, except that the entrainment of low mixing ratio air into the PBL in the WP cases dramatically increases the magnitude of the patch-induced water vapor mixing ratio all the way to the surface (Figure 6.20). The continuous growth in scale and magnitude of the scalar phase-averaged fields  $(\theta_{vp}, q_p)$  with increasing  $\lambda/z_i$  contrasts sharply with the variation of the dynamical fields  $(u_p, w_p)$  found in Figure 6.19.

#### 6.2.4.3 Scalar fluxes

In Section 6.1.3.2, it is shown that heterogeneity has little effect on the total horizontally-averaged vertical scalar flux profiles, however how the patch-induced circulation contributes

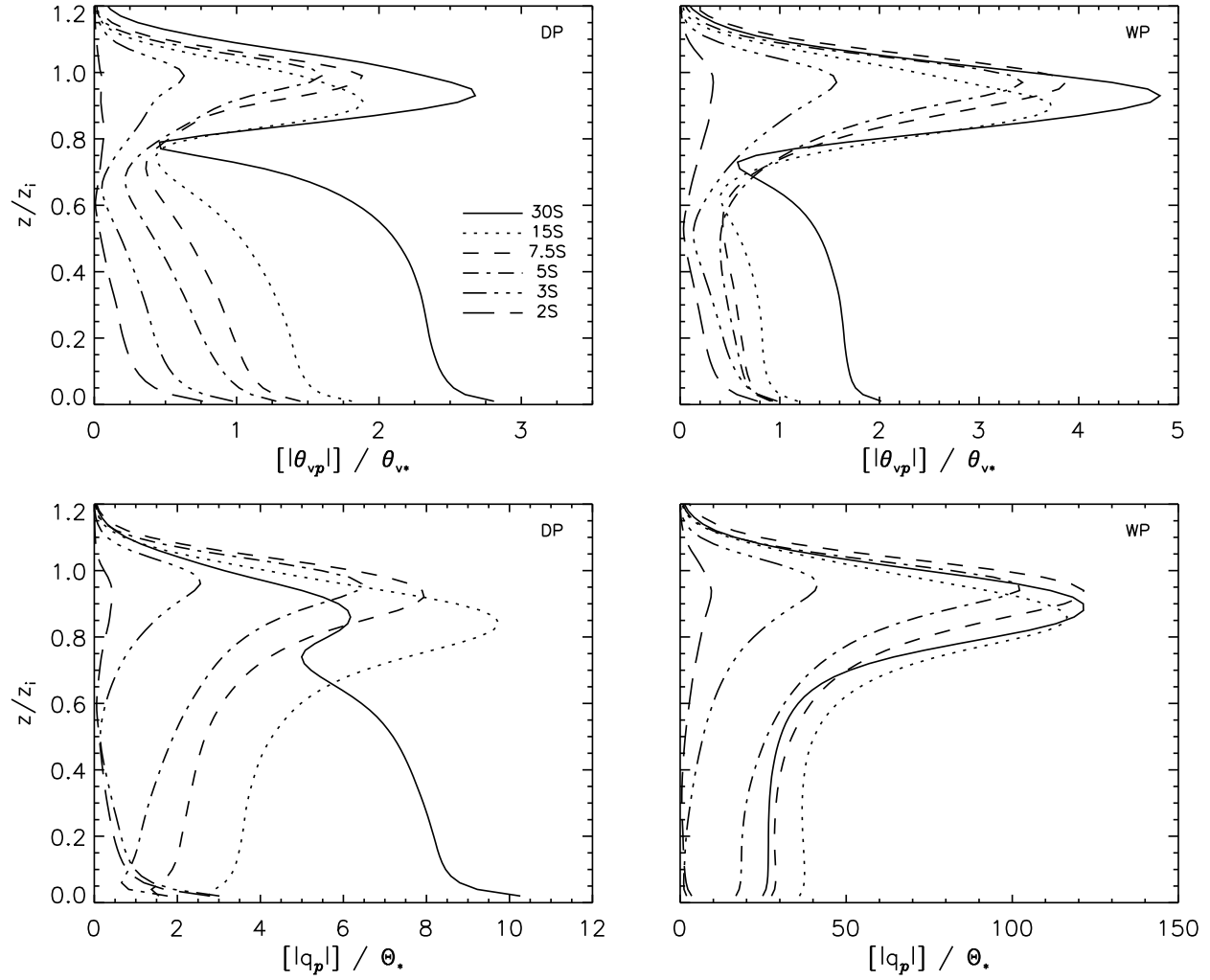


Figure 6.20: The normalized  $x$ -average of phase-correlated virtual potential temperature ( $[\theta_{vp}]/\theta_{v*}$ ) and water vapor mixing ratio ( $[q_p]/\theta_*$ ) for all cases with heterogeneity. The left hand panels depict DP cases and the right hand panels WP cases.

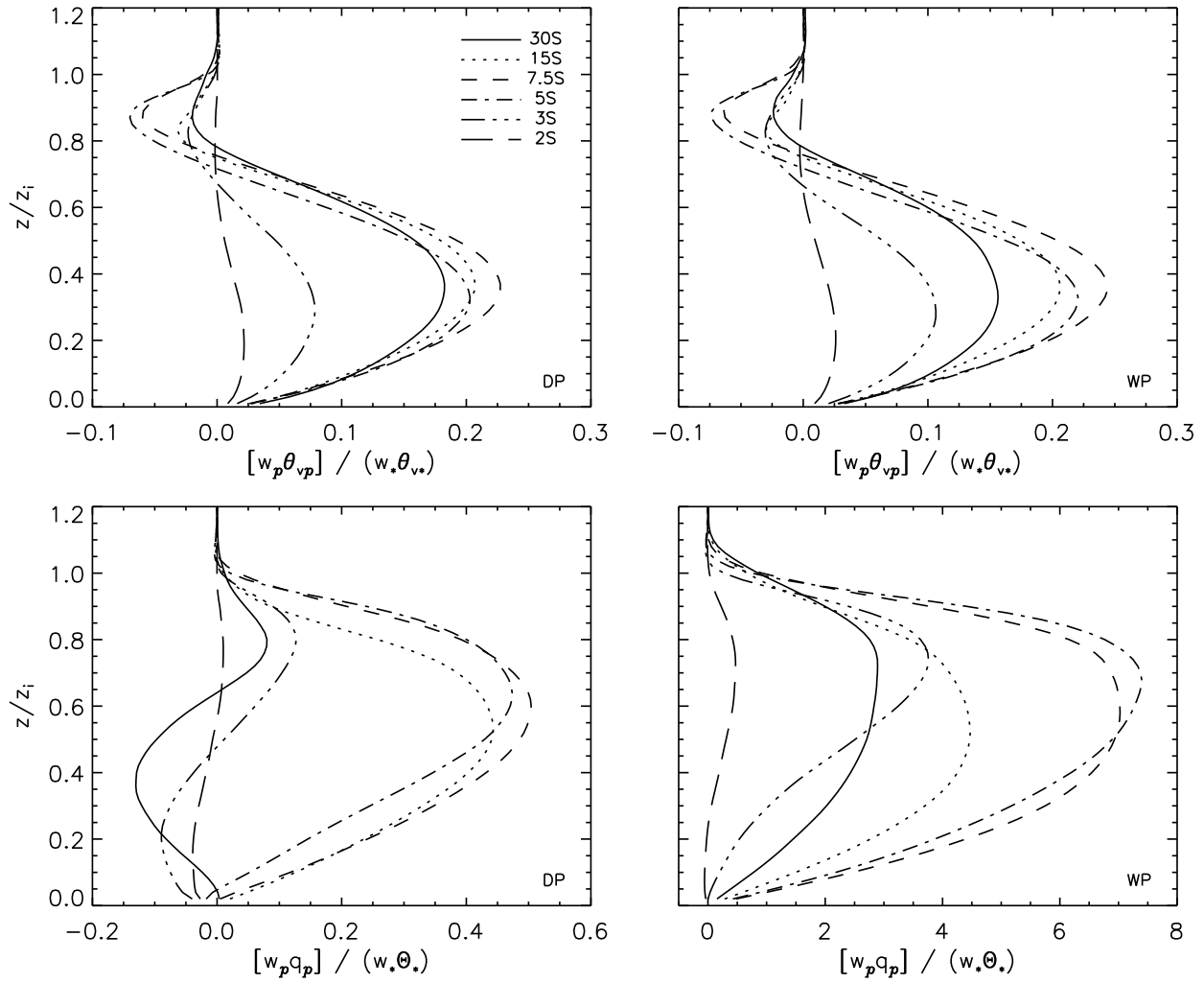


Figure 6.21: The normalized  $x$ -average of phase-correlated vertical virtual potential temperature flux ( $[w_p \theta_{vp}] / (w_* \theta_{v*})$ ) and vertical water vapor mixing ratio flux ( $[w_p q_p] / (w_* \Theta_*)$ ) for all cases with heterogeneity. The left hand panels depict DP cases and the right hand panels WP cases.

to the total fluxes can be quite different for varying patch size. For all heterogeneous cases with  $\lambda/z_i > 2$ , Figure 6.21 shows a significant contribution from the phase-correlated flow field to the virtual potential temperature flux; its contribution is positive in mid-PBL and negative near  $z_i$ , i.e., transporting high- $\theta_v$  upwards and low- $\theta_v$  downwards in mid-PBL and is also responsible for entrainment of  $\theta_v$ . Cases with  $\lambda/z_i < 2$  exhibit little contribution to the vertical flux of virtual potential temperature from the phase-correlated motion.

The patch-induced vertical water vapor mixing ratio fluxes are shown in the bottom panels of Figure 6.21. The organized motions in the  $4 < \lambda/z_i < 9$  cases (7.5S-15S) are the most significant, and the  $\lambda/z_i < 3$  cases are again less so. For DP-30S, the small-scale plumes which persist near the centers of each *dry* and *wet* patch, consist of both rising and sinking motions (see top right panel of Figure 6.14) that tend to cancel and hence provide a negligible amount of moisture flux. However for the WP environment, the large jump in water vapor mixing ratio across the inversion results in a moderate amount of moisture flux from the phase-induced motion.

Figures 6.22 and 6.23 present the contributions from the phase-correlated and un-correlated (background) turbulence to the total scalar flux for 30S, 7.5S and 3S cases. The total turbulent flux is  $\langle w''\theta_v'' + \tau_{w\theta_v} \rangle / \theta_{v*}$ ,  $\langle w''q'' + \tau_{wq} \rangle / \Theta_*$ , where the quantities ( )'' are resolved fluctuations and  $\tau$  is the subgrid-scale flux. In case WP-7.5S, the heterogeneity-induced cells contribute about  $\sim 70\%$  of the total virtual heat flux at  $z/z_i = 0.64$  (middle right panel of Figure 6.22). For most cases the background turbulence (dashed curves) contributes more than the phase-correlated motion (dotted curves) above  $z/z_i \sim 0.9$ , indicating that on average small-scale turbulence is ultimately responsible for entrainment. This finding is counter to the results from Zeng and Pielke (1995) and Seth and Giorgi (1996) who show that entrainment largely results from the mesoscale organized motions when using mesoscale models with parameterized PBL schemes.

For vertical water vapor fluxes, the 7.5S cases ( $\lambda/z_i \sim 4$ ) are dominated by the heterogeneity-induced organized motions in the upper half of the PBL for the DP case (middle left panel of Fig. 6.23) but throughout the whole PBL for the WP case (middle right panel of Figure 6.23). Averaged across the heterogeneity,  $w_p q_p / (w_* \Theta_*)$  in case DP-7.5S contributes a maximum of about 68% to the total flux at  $z/z_i \sim 0.7$ , while in the WP-7.5S case the phase-correlated component contributes almost 100% of the total flux throughout the PBL. The difference seen between these cases is largely due to the different moisture gradient across the entrainment interface. In the WP case, the organized motions intensify the moisture jump across the inversion over the dry soil (see Figure 6.18) which then enhances the contribution

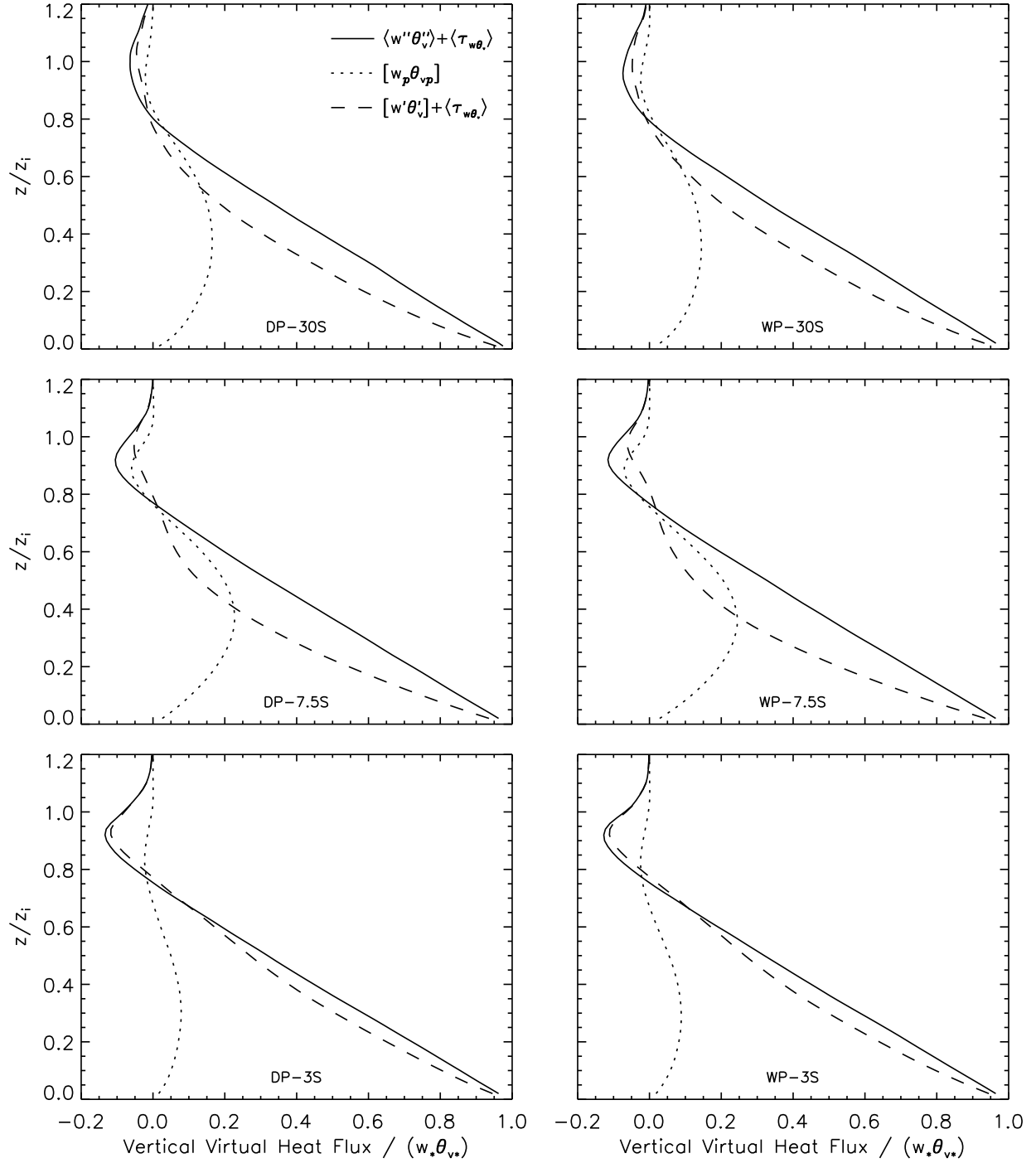


Figure 6.22: Vertical profiles of normalized total virtual heat flux  $(\langle w''\theta_v'' \rangle + \langle \tau_{w\theta_v} \rangle)/(w_*\theta_{v*})$ , the phase-correlated virtual heat flux  $[w_p\theta_{vp}]/(w_*\theta_{v*})$ , and background turbulent virtual heat flux  $([w'\theta_v'] + \langle \tau_{w\theta_v} \rangle)/(w_*\theta_{v*})$  for six cases. The left column are the DP cases, and the right column are the WP cases. The top row are the 30S cases, middle row are the 7.5S cases and the bottom row are the 3S cases.



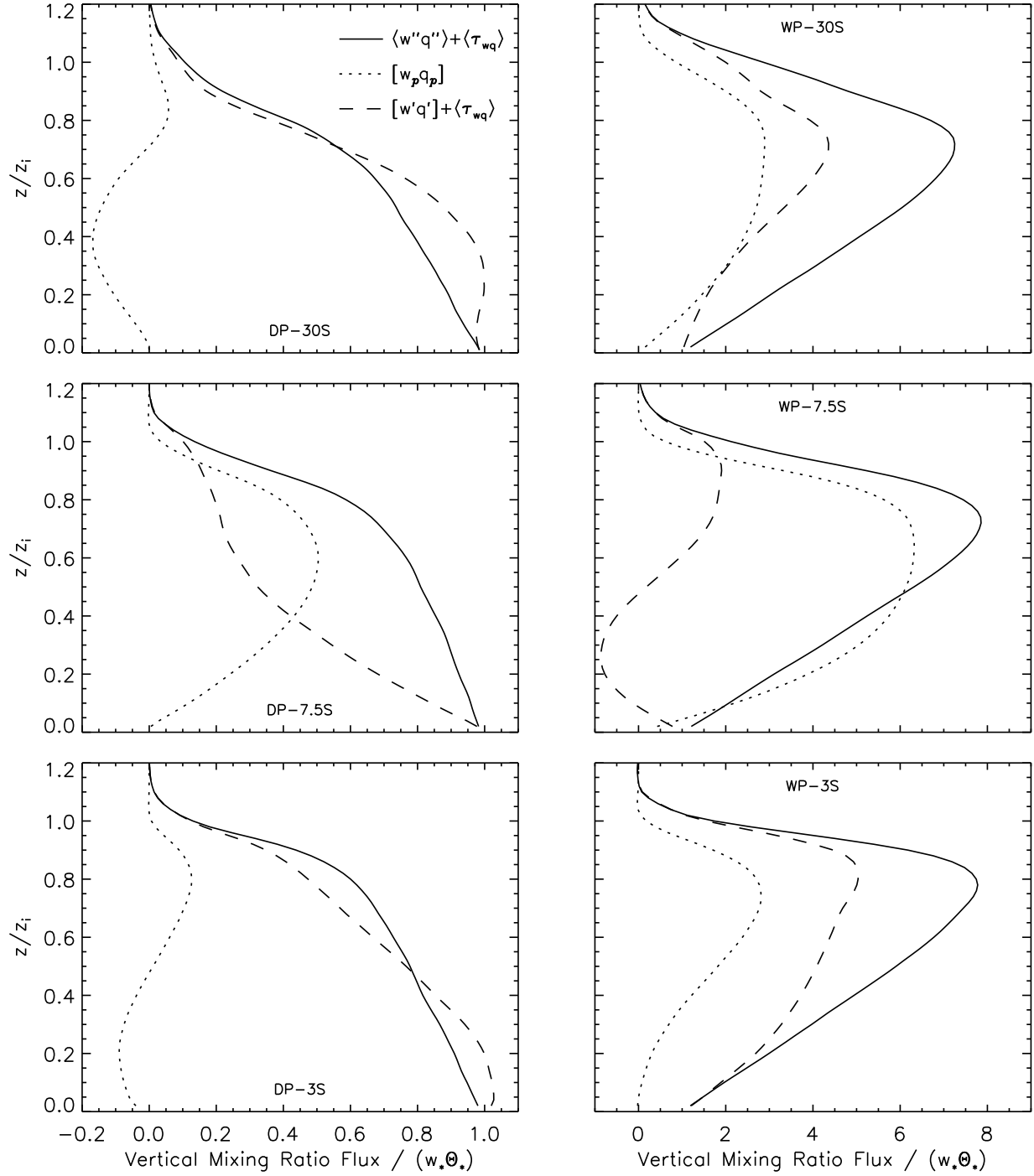


Figure 6.23: Vertical profiles of normalized total vertical mixing ratio flux  $(\langle w''q'' \rangle + \langle \tau_{wq} \rangle)/(w_*\Theta_*)$ , the phase-correlated mixing ratio flux  $[w_p q_p]/(w_*\Theta_*)$ , and background turbulent mixing ratio flux  $([w'q'] + \langle \tau_{wq} \rangle)/(w_*\Theta_*)$  for six cases. The left column are the DP cases, and the right column are the WP cases. The top row are the 30S cases, middle row are the 7.5S cases and the bottom row are the 3S cases.

of the organized motions to the vertical flux of  $wq$ . For both DP-30S and DP-3S cases, the phase-correlated component of the vertical mixing ratio flux is nearly zero, while both WP-30S and WP-3S show moderate contributions (Figure 6.23).

### 6.2.5 Impact of organized motions on point measurements

Vertical scalar fluxes are one of the primary quantities deduced from observations collected from fixed towers and platforms. Most often, vertical scalar flux is not directly measured but is instead computed from independent measurements of vertical velocity and the scalar of interest. The quality of the vertical flux estimate thus depends crucially on accurate measurements of  $w$ . In the field, sensors are rarely perfectly deployed and therefore observationalists typically apply some sort of a tilt correction that forces the time-average of  $w$  measured at a point to zero (*e.g.*, Dyer, 1981; Baldocchi et al., 1988; Berger et al., 2001; Finnigan et al., 2003). For example, Dyer (1981) notes that estimates of vertical momentum flux are corrected by about 14% per degree of tilt, while Baldocchi et al. (1988) reports a smaller scalar flux correction (about 3% per degree of tilt). The practice of forcing average vertical velocity to zero while justifiable for horizontally homogeneous flows becomes uncertain in the presence of surface heterogeneity (*e.g.*, Finnigan et al., 2003). The question we wish to address with our simulations is what are the possible consequences of assuming time average  $w = 0$  at a fixed point for scalar flux in the presence of heterogeneous surface conditions.

The analysis thus far has taken advantage of horizontal- and time-averaging to determine ensemble average quantities  $\langle \rangle$  and homogeneity in the  $y$ -direction to determine the phase-correlated quantities, *e.g.*,  $w_p$ . Tower measurements, however, are limited to measuring at a number of single points in time. In Figure 6.24, the lines with filled circles ( $\bullet$ ) are profiles of  $w_p/w_*$  at fixed  $x/\lambda$  of (0 or 1, 0.25, 0.5, 0.75) from case DP-7.5S, which are taken from the middle-right panel of Figure 6.14. The hatched regions in Figure 6.24 show plus and minus one standard deviation of  $w_p/w_*$  from the  $y$ -average. Therefore, at any  $y$ -location a measurement taken at one of the four  $x/\lambda$  ‘sites’ would encounter a heterogeneity-induced vertical velocity with magnitude and direction that most likely falls in the hatched-region. To emphasize this point, the open-boxed lines ( $\square$ ) in Figure 6.24 show profiles of normalized time-averaged vertical velocity,  $\{w\}/w_*$ , which are taken from a fixed  $y$ -location (the middle of the domain), the same four  $x/\lambda$ -locations, and averaged over the same length of time as

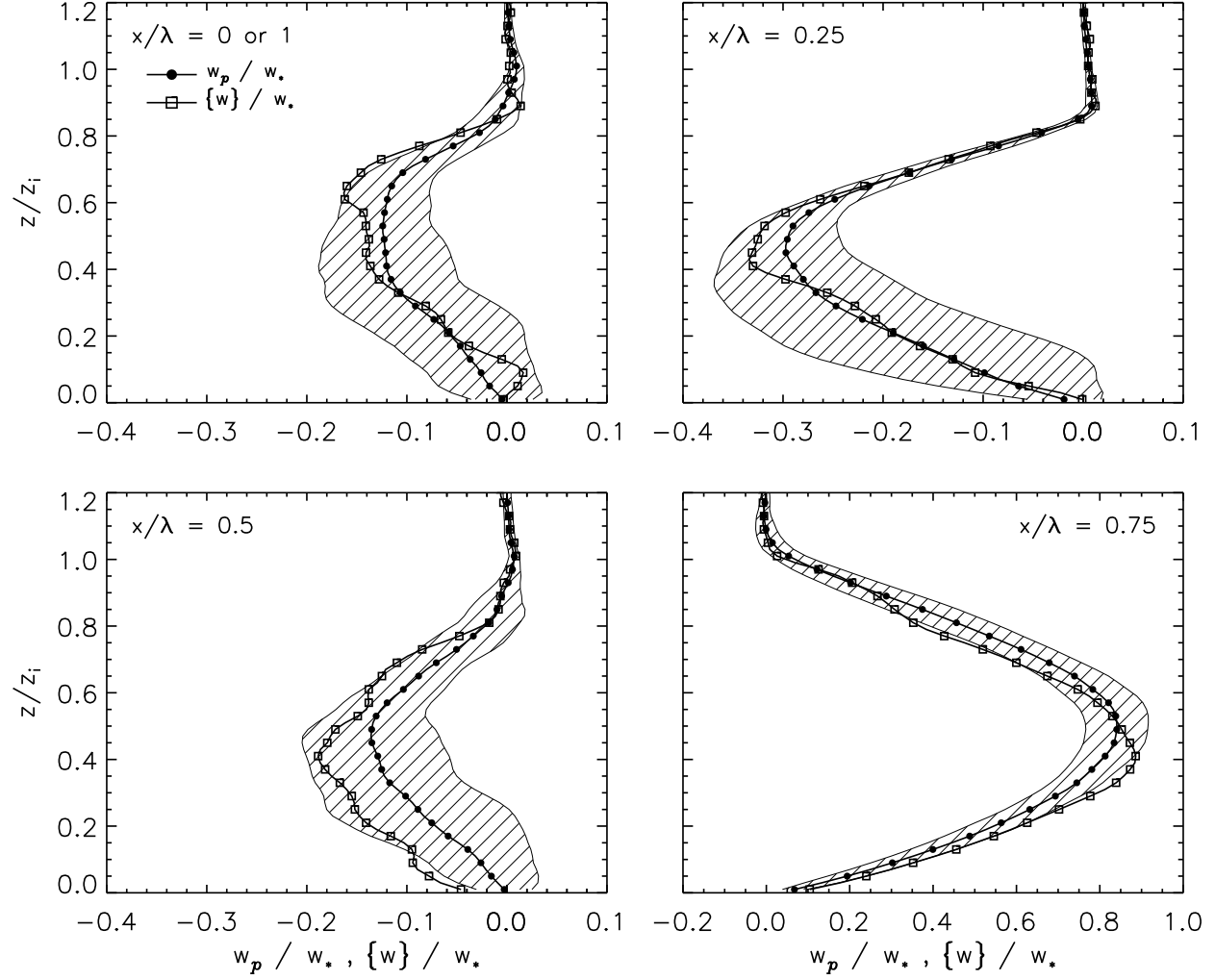


Figure 6.24: Vertical profiles of normalized phase-correlated vertical velocity ( $w_p/w_*$ ,  $\bullet$ ), and time-averaged vertical velocity ( $\{w\}/w_*$ ,  $\square$ ) at fixed  $x/\lambda$  for case DP-7.5S. The (top-left, top-right, lower-left, lower-right) panels represent locations  $x/\lambda = (0 \text{ or } 1, 0.25, 0.5, 0.75)$ . The hatch marks demarcate plus and minus one standard deviation of  $w_p/w_*$  from the  $y$ -average. Note the scale difference on the abscissa of the  $x/\lambda = 0.75$  plot.

the rest of the results presented in this manuscript<sup>§</sup>.

So, under free convective conditions like we've simulated, any coordinate rotation attempting to force the mean vertical velocity to zero will introduce dramatic errors. The magnitude and direction of these errors depends on the measurement height and location,  $z/z_i$  and  $x/\lambda$ , and on the heterogeneity scale,  $\lambda/z_i$  (compare the  $x/\lambda$  and  $z/z_i$  variation of  $w_p/w_*$  in Figures 6.19 and 6.14). And, as suggested by Finnigan et al. (2003), invoking longer time-averages when performing the rotations will not correct for heterogeneity-induced motions such as those discussed here.

To further emphasize the importance of the phase-correlated organized motions on point measurements, we compare three vertical profiles in Figure 6.25: 1) the total flux, 2) the background contribution to this total flux, and 3) fluxes calculated from time averages at a point. The filled circles represent  $y$ - and time-average (denoted as  $\langle \rangle_{y,t}$ ) of the background turbulence component of the total vertical virtual potential temperature flux (denoted with a single prime  $'$  as defined in Equation 6.1). The hatched areas represent plus and minus one standard deviation of these  $y$ - and time-averaged quantities as they vary in the  $y$ -direction. The time-averaged profiles are calculated from point data saved every ten time steps, averaged over the same length of time as the ensemble averaged data (4-10 turnover times). In this case, the fluxes are calculated using the following rule,  $\{w^\circ f^\circ\} = \{wf\} - \{w\}\{f\}$ , where  $f$  is any scalar and  $\{\}$  represents a time average at a fixed point over the 4-10 turnover times and  $^\circ$  is the deviation from that time average.

Time-averaged vertical virtual potential temperature fluxes obtained at individual  $x$  locations in a free-convective PBL with  $\lambda/z_i \sim 4$  heterogeneity differ from the total vertical flux (Figure 6.25). The magnitude and direction of the difference depends on the  $x/\lambda$  and  $z/z_i$  location of the point measurement. Over the *wet* soil at  $x/\lambda = 0.25$ , point flux measurements typically under-estimate the vertical virtual potential temperature flux throughout the vertical depth of the PBL. While over the center of the *dry* patch ( $x/\lambda = 0.75$ ), the point measurements over-estimate the vertical virtual potential temperature flux. For example, under free convective conditions a time-averaged point measurement at  $x/\lambda = 0.25$  and  $z/z_i = 0.1$  would under-estimate the vertical flux of virtual potential temperature by about 45% while the same measurement at  $x/\lambda = 0.75$  would over-estimate the flux by about 20%.

---

<sup>§</sup>We recognize that in the field, most averages occur over 15, 20, 30, or 60 minutes, but to compare with the other results presented in this manuscript, we average over the same 4-10 turnover times as the ensemble average results.

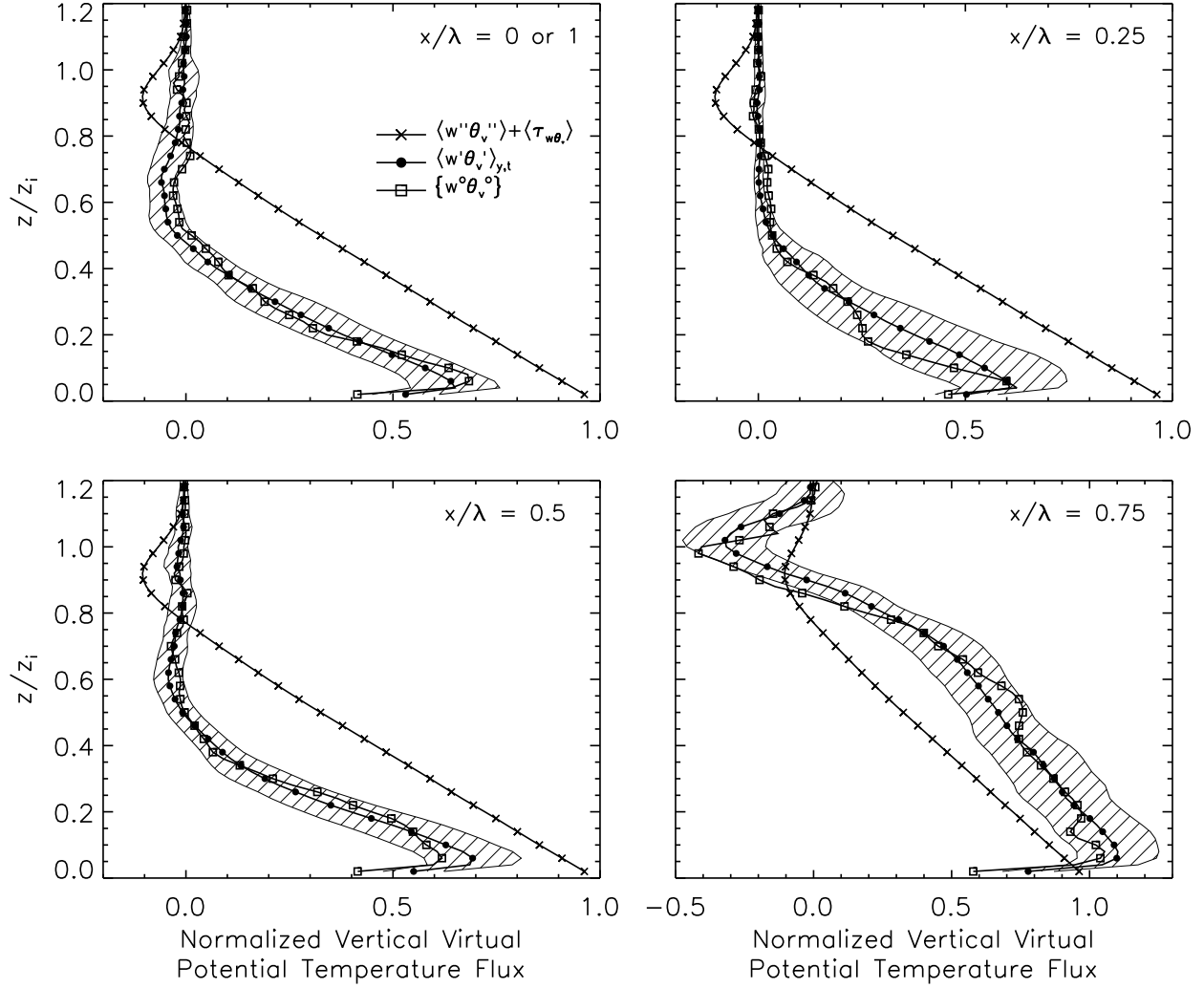


Figure 6.25: Vertical profiles of normalized vertical virtual potential temperature flux for case DP-7.5S. The  $\times$ -profile represents the the total flux,  $(\langle w''\theta_v'' \rangle + \langle \tau_{w\theta_v} \rangle) / (w_*\theta_{v*})$ . The  $\bullet$ -profile presents the background turbulent contribution,  $\langle w'\theta_v' \rangle_{y,t} / (w_*\theta_{v*})$ , and the hatch marks demarcate plus and minus one standard deviation of  $\langle w'\theta_v' \rangle_{y,t} / (w_*\theta_{v*})$  from the  $y$ -average. The  $\square$ -profile is the time-average at each  $x/\lambda$  and  $z/z_i$  location at  $y = L_y/2$ . The (top-left, top-right, lower-left, lower-right) panels represent locations  $x/\lambda = (0 \text{ or } 1, 0.25, 0.5, 0.75)$ . See the discussion in Section 6.2.5 for further explanation of how these quantities are calculated.

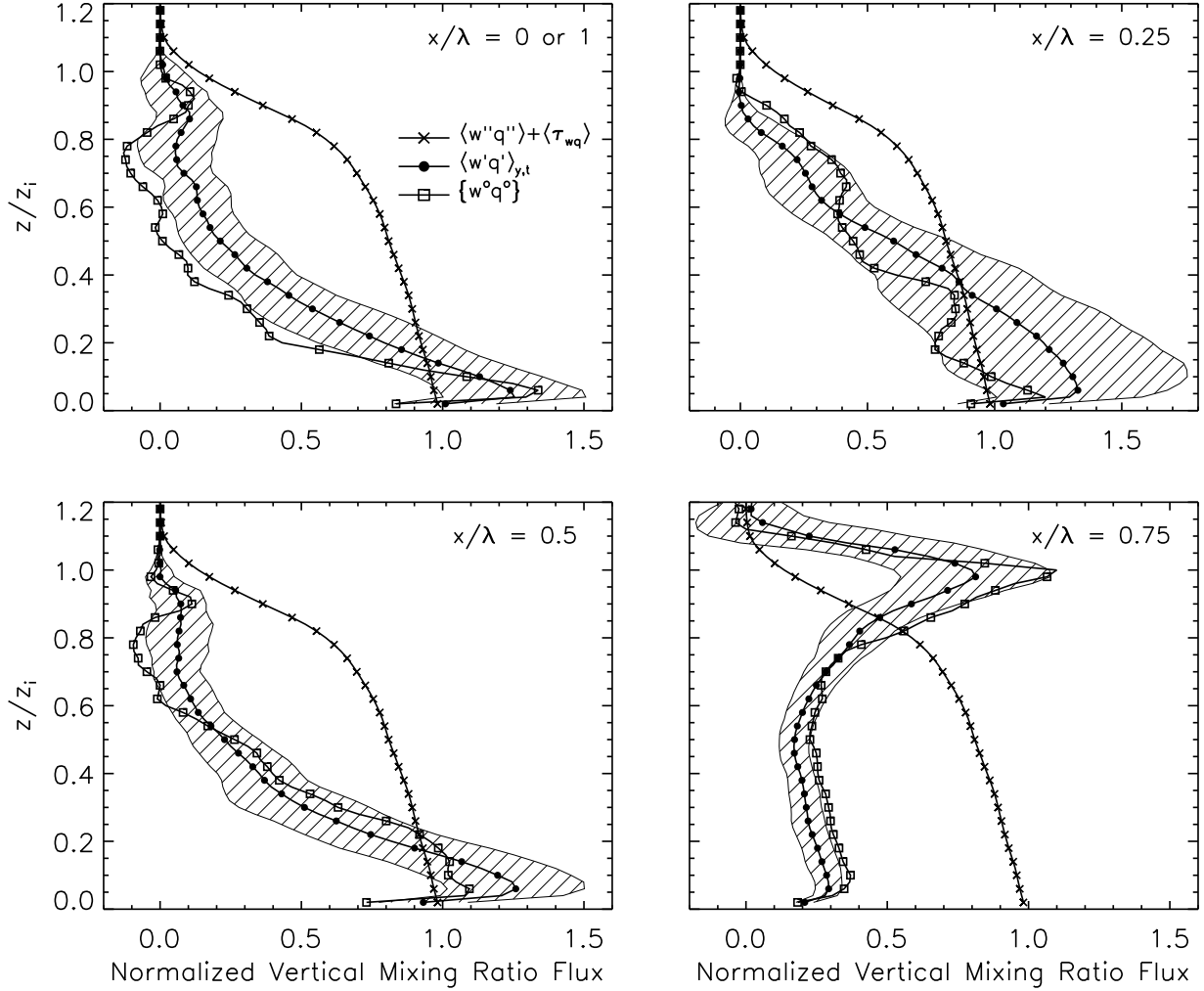


Figure 6.26: Vertical profiles of normalized vertical water vapor mixing ratio flux for case DP-7.5S. The  $\times$ -profile represents the the total flux,  $(\langle w''q'' \rangle + \langle \tau_{wq} \rangle)/(w_*\Theta_*)$ . The  $\bullet$ -profile presents the background turbulent contribution,  $\langle w'q' \rangle_{y,t}/(w_*\Theta_*)$ , and the hatch marks demarcate plus and minus one standard deviation of  $\langle w'q' \rangle_{y,t}/(w_*\Theta_*)$  from the  $y$ -average. The  $\square$ -profile is the time-average at each  $x/\lambda$  and  $z/z_i$  location at  $y = L_y/2$ . The (top-left, top-right, lower-left, lower-right) panels represent locations  $x/\lambda = (0 \text{ or } 1, 0.25, 0.5, 0.75)$ . See the discussion in Section 6.2.5 for further explanation of how these quantities are calculated.

Combined analysis of the middle left panel of Figure 6.16 and Figure 6.25, suggests that most of the vertical virtual potential temperature flux occurs over the *dry* patch (between  $0.6 < x/\lambda < 0.9$ , not shown). These figures also suggest that for the DP-7.5S case, the majority of the entrainment also occurs in this same region of  $x/\lambda$ , between 0.6 and 0.9<sup>¶</sup>.

For DP-7.5S, surrogate point measurements of vertical mixing ratio flux are given in Figure 6.26. Over the *wet* patch ( $x/\lambda=0.25$ ), below  $z/z_i \sim 0.4$ , point measurements over-estimate the vertical flux, while above this height, such measurements under-estimate the flux. Over the *dry* patch ( $x/\lambda=0.75$ ), point measurements dramatically under-estimate the vertical mixing ratio flux below  $z/z_i \sim 0.8$ , while above this level, point measurements over-estimate the entrainment of dry air from above. To quantify the influence near the surface, under free convective conditions a time-averaged point measurement at  $x/\lambda = 0.25$  and  $z/z_i = 0.1$  would over-estimate the vertical flux of water vapor mixing ratio by about 3% while the same measurement at  $x/\lambda = 0.75$  would under-estimate the flux by about 60%.

We caution the reader regarding the conclusions made from Figures 6.25 and 6.26 for the following reasons: 1) these figures are representative for a single heterogeneity scale ( $\lambda/z_i \sim 4$ ), and 2) these conclusions may not apply to convective PBLs with mean wind. Point measurements assume that numerous energy-containing eddies advected by the mean wind are sampled over the averaging time-period (Kaimal and Finnigan, 1994). Since our simulations are of free convection, the point measurements simulated here continuously sample within the same stationary eddy, *i.e.*, the heterogeneity-induced organized motion. This analysis will have much greater meaning when we include wind in the simulations.

---

<sup>¶</sup>Note that for the background turbulence component of the entrainment, we only show the single profile in Figure 6.25, but that inspection of  $x/\lambda$  versus  $z/z_i$  plots of  $\langle w'\theta'_v \rangle / (w_*\theta_{v*})$  points to this result.





## Chapter 7

### Summary and Conclusions

We have developed a large-eddy simulation code coupled with a fully interactive land-surface model. Initial temperature and moisture conditions are specified for the PBL and the soil and are taken from SGP97 measurements. No mean wind is imposed such that the incoming solar radiation is the only external forcing in the simulations. The results show that soil moisture content is a crucial variable influencing PBL motions.

Visualizations of instantaneous fields reveal the signature of cellular convection at the surface and in the soil. Instantaneous slices of the PBL show dramatic modification of the PBL structure resulting from soil moisture heterogeneity. Instantaneous surface fluxes also depict the dynamic response of the forcing to the PBL.

Consistent with previous research, under free convective conditions, heterogeneity generates organized motions. Heterogeneity at scales ranging from  $\lambda/z_i \sim 4-9$  induces the greatest PBL response. The organized motions induced at these scales of heterogeneity decrease the exchange coefficients for (momentum, scalars) by about (6, 9)% compared to the homogeneous average soil cases (AS), and increase the bulk turbulence kinetic energy of the PBL by about 20%. The generation of these organized motions and the subsequent increase in turbulence kinetic energy, however, do not dramatically influence entrainment rates.

Implications from these findings are that large-scale models that cannot resolve land-surface heterogeneity will slightly underestimate the surface fluxes of heat and moisture, but should not mis-estimate PBL entrainment. With respect to surface-layer turbulence statistics, heterogeneity makes the buoyantly forced PBLs appear more like mixed shear-buoyancy PBLs due to the induced organized motions.

Phase-averaged statistics reveal that the rising motion over the *dry* side of the heterogeneity is narrower in space and larger in magnitude compared to the sinking motion over

the *wet* side. In other words, the patch-induced vertical velocity field is strongly skewed. The importance of the organized motions differs for dynamical and scalar fields, and depends on the scale of the heterogeneity  $\lambda$ , the boundary layer height  $z_i$ , and the initial moisture state of the PBL. Heterogeneity at scales  $4 < \lambda/z_i < 9$  induces the largest organized flow fields ( $[u_p^2], [w_p^2]$ ). Small-scale heterogeneity ( $\lambda/z_i < 3$ ) tends to eliminate the ability for the induced organized motions to transport water vapor, and in these cases a heterogeneous surface has little effect on the vertical transport. For  $\lambda/z_i > 9$ , the patch-size motion is too broad to sustain and the heterogeneity instead allows small scale plumes to develop near the center of each patch and hence smaller phase-correlated velocity variances are induced. However, the organized components of the scalar fields (potential temperature and mixing ratio) grow continuously in magnitude and scale as  $\lambda/z_i$  increases. Compared to water vapor mixing ratio, virtual potential temperature is less influenced by the organized motions. Water vapor mixing ratio is largely transported by the organized motions and thus depends critically on the nature of the surface heterogeneity. For example, the DP-7.5S case produces a larger amount of water vapor mixing ratio in the PBL over the *dry* soil than over the *wet* soil, but in DP-30S the PBL has a larger mixing ratio over the *wet* soil than over the *dry* soil.

As a result, fixed-point measurements of vertical scalar flux (*i.e.*, made from a tower) are prone to error if the measurement occurs within a region of heterogeneity. The magnitude and direction of the error depends on the location of the measurement with respect to the underlying land-surface heterogeneity and on the quantity in question. For example, under free convective conditions a time-averaged point measurement at  $x/\lambda = 0.25$  and  $z/z_i = 0.1$  would over-estimate the vertical water vapor mixing ratio flux by about 3% while the same measurement at  $x/\lambda = 0.75$  would under-estimate the flux by about 60%.

## Acknowledgements:

NCAR is sponsored by the National Science Foundation. This work was supported in part by the NASA Land Surface Hydrology program through contract NAG5-8839. We thank Michael Ek from NCEP for supplying us with the NOAH land surface model and for helpful discussions, and Don Lenschow and Peggy Lemone for comments on an earlier version of this manuscript.

# Appendix A

## Numerics

For all variables the LES uses pseudo-spectral differencing in the horizontal. For velocities, the LES uses second-order centered-in-space differencing, while for scalars the monotone advection scheme of Koren (1993) is used. Spalart et al.'s (1991) third-order Runge-Kutta scheme advances all fields in time using a fixed Courant-Friedrichs-Lewy (CFL) number of 0.63 for a complete 3-stage time step. Periodic boundary conditions are imposed in the horizontal. To allow the propagation of gravity waves out of the top of the domain, the upper boundary condition is that of Klemp and Durran (1983). Because the LES uses spectral differencing in the horizontal, the MPI implementation breaks up the domain in the vertical into slabs of horizontal data residing on a single processor. To perform the spectral decomposition, we use NCAR's FFTPACK version 4.1 (<http://www.scd.ucar.edu/softlib/FFTPACK.html>).

In the LSM, upwind finite differences are used for vertical derivatives and the Crank-Nicholson scheme is used for time differencing. At the lower boundary, the hydraulic diffusivity is assumed to be zero so that the soil water flux is determined solely by gravitational conduction. The soil heat flux is computed from a vertical temperature gradient between the lowest LSM model level and a specified soil temperature at an imaginary grid point one meter below the bottom of the model. Further details can be found in Mahrt and Pan (1984), Pan and Mahrt (1987), and Chang et al. (1999). To improve scalability when solving the LSM for the coupled surface boundary condition, we use MPI to break up the calculation in the  $x$ -direction.



# Bibliography

- Albertson, J. D., W. P. Kustas, and T. M. Scanlon, 2001: ‘Large-eddy simulation over heterogeneous terrain with remotely sensed land surface conditions’, *Water Resour. Res.*, **37**, 7, 1939–1953.
- Albertson, J. D. and M. B. Parlange, 1999: ‘Natural integration of scalar fluxes from complex terrain’, *Adv. Water Resour.*, **23**, 239–252.
- Avisar, R. and T. Schmidt, 1998: ‘An evaluation of the scale at which ground-surface heat flux patchiness affects the convective boundary layer using large-eddy simulations’, *J. Atmos. Sci.*, **55**, 2666–2689.
- Baldocchi, D. D., B. B. Hicks, and T. P. Meyers, 1988: ‘Measuring biosphere-atmosphere exchanges of biologically related gases with micrometeorological methods’, *Ecology*, **69**, 1331–1340.
- Berger, B. W., K. J. Davis, C. Yi, P. S. Bakwin, and C. Zhao, 2001: ‘Long-term carbon dioxide fluxes from a very tall tower in a northern forest: Part I. Flux measurement methodology’, *J. Atmos. Oceanic Tech.*, **18**, 529–542.
- Brubaker, K. L. and D. Entekhabi, 1996: ‘Analysis of feedback mechanisms in land-atmosphere interaction’, *Water Resour. Res.*, **32**, 5, 1343–1357.
- Brutsaert, W., 1982: *Evaporation into the Atmosphere*, Kluwer Academic Publishers, Dordrecht, The Netherlands, 299pp pp.
- Chang, S., D. Hahn, C.-H. Yang, and D. Norquist, 1999: ‘Validation of the CAPS model land surface scheme using the 1987 Cabauw/PILPS dataset’, *J. Appl. Meteorol.*, **38**, 405–422.
- Davis, K. J., N. Gamage, C. R. Hagelberg, C. Kiemle, D. H. Lenschow, and P. P. Sullivan, 2000: ‘An objective method for deriving atmospheric structure from airborne LIDAR observations’, *J. Atmos. Oceanic Tech.*, **17**, 1455–1468.

- Deardorff, J. W., 1979: 'Prediction of convective mixed-layer entrainment for realistic capping inversion structure', *J. Atmos. Sci.*, **36**, 424–436.
- Dyer, A. J., 1981: 'Flow distortion by supporting structures', *Boundary-Layer Meteorol.*, **20**, 243–251.
- Esau, I. N. and T. J. Lyons, 2002: 'Effect of sharp vegetation boundary on the convective atmospheric boundary layer', *Agric. For. Meteorol.*, **114**, 3–13.
- Finnigan, J. J., R. Clement, Y. Malhi, R. Leuning, and H. Cleugh, 2003: 'A re-evaluation of long-term flux measurement techniques. Part I: Averaging and coordinate rotation', *Boundary-Layer Meteorol.*, **107**, 1–48.
- Garratt, J. R., 1993: 'Sensitivity of climate simulations to land-surface and atmospheric boundary-layer treatments - A review', *J. Clim.*, **6**, 419–448.
- Glendening, J. W., 1996: 'Lineal eddy features under strong shear conditions', *J. Atmos. Sci.*, **53**, **23**, 3430–3449.
- Hadfield, M. G., W. R. Cotton, and R. A. Pielke, 1991: 'Large-eddy simulations of thermally forced circulation in the convective boundary layer. Part I: A small scale circulation with zero wind', *Boundary-Layer Meteorol.*, **57**, 79–114.
- Hechtel, L. M., C.-H. Moeng, and R. B. Stull, 1990: 'The effects of nonhomogeneous surface fluxes on the convective boundary layer: A case study using large-eddy simulation', *J. Atmos. Sci.*, **47**, 1721–1741.
- Hussain, A. K. M. F. and W. C. Reynolds, 1970: The mechanics of an organized wave in turbulent shear flows, *J. Fluid Mech.*, **41**, 241–258.
- Kaimal, J. C. and J. J. Finnigan, 1994: *Atmospheric Boundary Layer Flows: Their Structure and Measurement*, Oxford University Press, New York, 289 pp.
- Khanna, S. and J. G. Brasseur, 1998: 'Three-dimensional buoyancy- and shear-induced local structure of the atmospheric boundary layer', *J. Atmos. Sci.*, **55**, 710–743.
- Klemp, J. B. and D. R. Durran, 1983: 'An upper boundary condition permitting internal gravity wave radiation in numerical mesoscale models', *Mon. Wea. Rev.*, **111**, 430–444.

- Komminaho, J., A. Lundblad, and A. V. Johansson, 1996: ‘Very large structures in plane turbulent Couette flow’, *J. Fluid Mech.*, **320**, 259–285.
- Koren, B., 1993: ‘A robust upwind discretization method for advection, diffusion and source terms’, in *Numerical Methods for Advection-Diffusion Problems*, edited by C. B. Vrengdenhil and B. Koren, volume 45 of *Notes on Numerical Fluid Mechanics*, chapter 5, pp. 117–138, Vieweg Verlag, Braunschweig, Germany.
- Kustas, W. P. and J. D. Albertson, 2003: ‘Effects of surface temperature contrast on land-atmosphere exchange: A case study from Monsoon 90’, *Water Resour. Res.*, **39**, 6, 1159–1174.
- Lilly, D. K., 2002: ‘Entrainment into mixed layers. Part I: Sharp-edged and smoothed tops’, *J. Atmos. Sci.*, **59**, 3340–3352.
- Lin, C.-L., J. C. McWilliams, C.-H. Moeng, and P. P. Sullivan, 1996: ‘Coherent structures and dynamics in a neutrally stratified planetary boundary layer flow’, *Phys. Fluids*, **8**, 10, 2626–2639.
- Mahrt, L., 1998: ‘Flux sampling errors for aircraft and towers’, *J. Atmos. Oceanic Tech.*, **15**, 416–429.
- Mahrt, L. and H. Pan, 1984: ‘A two-layer model of soil hydrology’, *Boundary-Layer Meteorol.*, **29**, 1–20.
- Mahrt, L., D. Vickers, and J. Sun, 2001a: ‘Spatial variations of surface moisture flux from aircraft data’, *Adv. Water Resour.*, **24**, 1133–1141.
- Mahrt, L., D. Vickers, J. Sun, N. O. Jensen, H. Jørgensen, E. Pardyjak, and H. Fernando, 2001b: ‘Determination of the surface drag coefficient’, *Boundary-Layer Meteorol.*, **99**, 249–276.
- McNaughton, K. G. and M. R. Raupach, 1996: ‘Responses of the convective boundary layer and the surface energy balance to large-scale heterogeneity’, in *Scaling up in Hydrology using Remote Sensing*, edited by J. B. Stewart, E. T. Engman, R. A. Feddes, and Y. Kerr, pp. 171–182, John Wiley & Sons, Chichester.
- Moeng, C.-H., 1984: ‘A large-eddy simulation model for the study of planetary boundary-layer turbulence’, *J. Atmos. Sci.*, **41**, 2052–2062.

- Moeng, C.-H. and P. P. Sullivan, 1994: 'A comparison of shear- and buoyancy-driven planetary boundary layer flows', *J. Atmos. Sci.*, **51**, 999–1022.
- Nieuwstadt, F. T. M., P. J. Mason, C.-H. Moeng, and U. Schumann, 1993: 'Large-eddy simulation of the convective boundary layer: A comparison of four computer codes', in *Turbulent Shear Flows 8*, edited by F. Durst, R. Friedrich, B. E. Launder, F. W. Schmidt, U. Schumann, and J. H. Whitelaw, Springer-Verlag, Berlin.
- Pan, H.-L. and L. Mahrt, 1987: 'Interaction between soil hydrology and boundary layer development', *Boundary-Layer Meteorol.*, **38**, 185–202.
- Paulson, C. A., 1970: 'The mathematical representation of wind speed and temperature profiles in the unstable atmospheric surface layer', *J. Appl. Meteorol.*, **9**, 857–861.
- Raasch, S. and G. Harbusch, 2001: 'An analysis of secondary circulations and their effects caused by small-scale surface heterogeneities using large-eddy simulation', *Boundary-Layer Meteorol.*, **101**, 31–59.
- Raupach, M. R., 2000: 'Equilibrium evaporation and the convective boundary layer', *Boundary-Layer Meteorol.*, **96**, 107–141.
- Rowntree, P. R. and J. Bolton, 1983: 'Simulation of the atmospheric response to soil moisture anomalies over Europe', *Quart. J. Roy. Meteorol. Soc.*, **109**, 501–526.
- Roy, S. B. and R. Avissar, 2000: 'Scales of response of the convective boundary layer to land-surface heterogeneity', *Geophys. Res. Lett.*, **27**, 533–536.
- Schlichting, H., 1979: *Boundary-Layer Theory*, McGraw-Hill, Inc., New York, 817 pp.
- Schmidt, H. and U. Schumann, 1989: 'Coherent structure of the convective boundary layer derived from large-eddy simulation', *J. Fluid Mech.*, **200**, 511–562.
- Segal, M. and R. W. Arritt, 1992: 'Nonclassical mesoscale circulations caused by surface sensible heat-flux gradients', *Bull. Amer. Meteorol. Soc.*, **73**, **10**, 1593–1604.
- Seth, A. and F. Giorgi, 1996: 'Three-dimensional model study of organized mesoscale circulations induced by vegetation', *J. Geophys. Res.*, **101**, **D3**, 7371–7391.



- Shen, S. and M. Y. Leclerc, 1995: ‘How large must surface inhomogeneities be before they influence the convective boundary layer structure? A case study’, *Quart. J. Roy. Meteorol. Soc.*, **121**, 1209–1228.
- Spalart, P. R., R. D. Moser, and M. M. Rogers, 1991: ‘Spectral methods for the Navier-Stokes equations with one infinite and two periodic directions’, *J. Comp. Phys.*, **97**, 297–324.
- Sullivan, P. P., J. C. McWilliams, and C.-H. Moeng, 1996: ‘A grid nesting method for large-eddy simulation of planetary boundary-layer flows’, *Boundary-Layer Meteorol.*, **80**, 167–202.
- , 2000: ‘Simulation of turbulent flow over idealized water waves’, *J. Fluid Mech.*, **404**, 47–85.
- Sullivan, P. P., C.-H. Moeng, B. Stevens, D. H. Lenschow, and S. D. Mayor, 1998: ‘Structure of the entrainment zone capping the convective atmospheric boundary layer’, *J. Atmos. Sci.*, **55**, 3042–3064.
- Weaver, C. P. and R. Avissar, 2001: ‘Atmospheric disturbances caused by human modification of the landscape’, *Bull. Amer. Meteorol. Soc.*, **82**, **2**, 269–281.
- Willis, G. E. and J. W. Deardorff, 1974: ‘A laboratory model of the unstable planetary boundary layer’, *J. Atmos. Sci.*, **31**, 1297–1307.
- Zeng, X. and R. A. Pielke, 1995: ‘Landscape-induced atmospheric flow and its parameterization in large-scale numerical models’, *J. Clim.*, **8**, 1156–1177.